Journal of Sound and Vibration 547 (2023) 117527

Contents lists available at ScienceDirect

Journal of Sound and Vibration

journal homepage: www.elsevier.com/locate/jsvi

Multi-chamber micro-perforated panel absorbers optimised for high amplitude broadband absorption using a two-point impedance method

Jiayu Wang *, Gareth J. Bennett *

Department of Mechanical, Manufacturing and Biomedical Engineering, Trinity College Dublin, the University of Dublin, D02 PN40, Ireland

ARTICLE INFO

Keywords:
Micro-perforated panel absorber
Acoustic metamaterial
Low-frequency broadband sound absorption
Two-point impedance method
Optimisation

ABSTRACT

An optimised, multi-chamber, micro-perforated panel absorber (MC-MPPA) with micro-perforated adjoining panels is presented in this paper. An MPPA is a clean and efficient noise absorber with a simple structure making it an increasingly popular choice over porous material-based solutions. For the basic configuration, the bandwidth is typically limited by the perforation size and the frequency range by the backing cavity depth. In order to improve these parameters, innovative variations of the MPPA have been proposed in the literature, but the development of a solution which delivers both a broadband frequency response at low frequencies, with a shallow cavity has yet to appear. This paper proposes such a technological breakthrough by employing a graph-theory-based method to the MPPA problem. By using the two-point impedance method (TpIM) based on graph theory, a model for multi-chamber MPPAs which are coupled with each other in two dimensions through perforated side panels can be developed, an onerous task for standard equivalent circuit analysis due to the generation of non-planar circuits. The resulting model lends itself to optimisation and thus allows the differing geometric parameters of a tessellated network of chambers to be combined to maximise the sound absorption in a frequency range for a particular depth. An overall absorption coefficient of 0.83 can be achieved experimentally in the frequency range of 660 Hz to 2 kHz with an MC-MPPA of only 22 mm thick. In addition, when the air cavity depth is slightly increased to 50 mm, an overall absorption coefficient of greater than 0.82 can be achieved in the 281 Hz to 1 kHz frequency range. Experimentally, an absorption coefficient of approximately 0.82 is achieved at 340 Hz at an air cavity depth of 50 mm, which is a depth-to-wavelength ratio of 20, making the MC-MPPA a deeply subwavelength absorber. Results have been verified theoretically, numerically and experimentally.

1. Introduction

A micro-perforated panel absorber (MPPA) is a simple and highly versatile acoustic absorber [1–13]. Building on the theories of Rayleigh [14] and Crandall [15], Maa [1–3] first proposed a general theory and design of the MPPA as a useful noise absorbing technology in 1975. The sound absorption process is mainly due to viscous losses in an array of sub-millimetre holes [3,16]. The MPPA is more simple in structure compared to porous material-based metamaterials [17,18], and compared to membrane type acoustic metamaterials [19–22], they are more robust and less vulnerable to high temperatures. However, the sound absorption

* Corresponding authors.
E-mail addresses: wangj12@tcd.ie (J. Wang), gareth.bennett@tcd.ie (G.J. Bennett).

https://doi.org/10.1016/j.jsv.2022.117527
Received 30 April 2022; Received in revised form 15 November 2022; Accepted 15 December 2022
Available online 28 December 2022

bandwidth of traditional micro-perforated panel structures is limited. Thus, effective low-frequency and broadband sound absorption in a light, small form-factor micro-perforated panel structure is still a considerable challenge.

Extensive research has been conducted on MPPAs to improve their sound absorption properties. Multi-layer, or sandwich, MPPA structures have shown promise and have been explored repeatedly. Khosravani and Reinicke [23] proposed a three-layer MPPA design, which consists of a micro-perforated panel, a porous material layer and an air-back cavity. Their study employs advanced manufacturing techniques for processing micro-perforated panels and they examine the effect of the micro-perforated panel perforation ratio, porous materials and the air-back cavity depth on the acoustic properties of an MPPA measured by impedance tube experiments. Min and Guo [24] proposed a novel MPPA design, in which arrays of sub-cavities of different depths are periodically arranged in parallel behind a micro-perforated panel. This design achieves an average absorption coefficient of more than 0.5 and a maximum absorption coefficient of 0.98 in the frequency range from 450 to 3500 Hz, but the maximum cavity depth is up to 100 mm. Bucciarelli et al. [25] proposed a multi-layer MPPA design, where multiple micro-perforated panel layers are arranged in parallel and separated by multiple air gaps. Both five-layer and six-layer MPPA designs theoretically and experimentally demonstrated over 90% sound absorption in the frequency range from 400 Hz to 2000 Hz. However, the entire thickness of these MPPA designs is over 110 mm (five-layer MPPA) and over 132 mm (six-layer MPPA), respectively. Wang and Li [26] proposed an MPPA design of hybrid-arranged perforated panels with perforated partitions. Similar to Refs. [24,25], this design does improve the sound absorption of the MPPA but requires a deep air back cavity. Kim and Yoon [27] presented a new configuration of a perforated panel and applied a porous separating partition to extend the bandwidth of sound absorption. Numerical simulation results showed that this design successfully broadened the absorption bandwidth after optimisation. However, the addition of the porous material will undoubtedly increase the absorber's weight and as with all porous materials can absorb and hold water and dust. Carbajo et al. [28] proposed the design of an MPPA with micro-perforated partitions. This design achieved a broader bandwidth of sound absorption than traditional hard wall partitioned MPPAs.

Recently, there has also been interest in changing the shape or material of the micro-perforated panel and in adding active control. Wang and Liu [29] investigated the sound absorption properties of an MPPA with a corrugated micro-perforated panel. Experimental results showed that compared to an MPPA with a flat micro-perforated panel, the corrugated MPPA can significantly increase the sound absorption capacity at dips in the absorption curve. Kong et al. [30] investigated the sound absorption properties of an MPPA with a micro-perforated panel, made with a perforated polyvinylidene fluoride (PVDF) film. The advantage of this design is that it can be more compact and the acoustic performance can be adjusted with a change in voltage. Liu et al. [5] proposed a smart MPPA design by combining a flexible micro-perforated panel and a surface-bonded piezoelectric ceramic. This design improves the sound absorption of the MPPA by enhancing the vibration of the panel through the coupling between the panels and the surface-bonded piezoelectric ceramic. The addition of electronics to MPPAs, whilst potentially enhancing performance, inevitably increases complexity and weight and sensitivity to environmental conditions. Ren et al. [31] proposed an MPPA design where local resonators (LRs) were attached to a flexible micro-perforated panel. Numerical simulations show that the local resonance of flexible micro-perforated panels can achieve a sound absorption improvement.

Maa [3] stated as early as 1998, that reducing the perforation diameter of the micro-perforated panel to below 0.1 mm would allow the sound absorption limits of a single MPP to be achieved and thus widen its sound absorption bandwidth [32]. However, there has been very little research conducted in reducing the perforation diameter physically due to limitations in perforation processing technology. An exception in the literature is the work of Qian et al. [32] who employed MEMS (Micro-electromechanical systems) technology to create ultra-micro perforations down to 10s of microns and successfully confirmed a number of Maa hypotheses related to sub 0.1 mm perforations [3].

With the development of acoustic metamaterials, accurate analysis of acoustic systems becomes more and more critical. The equivalent circuit model (ECM) method [28,33] uses electrical circuits to characterise the operational parameters of an acoustic system. The ECM usually uses $\Delta - Y$ and $Y - \Delta$ transforms to simplify the circuit to estimate acoustic impedance. However, as the complexity of the acoustic system increases, the ECM becomes unmanageable. For this reason, Davis et al. [34] proposed a graph-theory approach, which is essentially the two-point impedance theory proposed by Tzeng and Wu [35], but used instead to estimate acoustic impedance. The sound absorption coefficient results obtained by this graph-theory-based approach were in good agreement with those obtained by numerical simulations. This initial study provided evidence of the great potential of the two-point impedance theory for complex acoustic analysis. In the current work, a two-point impedance method is developed and employed to further the state-of-the-art in MPPA research.

The main objectives of the current study are as follows: (1) to introduce the novel acoustic sound absorber, *viz.*, the multi-chamber, micro-perforated panel absorber (MC-MPPA) with micro-perforated internal panels; (2) to establish a graph-theory-based predictive analytical method, (TpIM), for optimising acoustic treatments; (3) to develop an optimised MC-MPPA with high amplitude, low-frequency and broadband sound absorption; (4) to validate both the proposed predictive analytical method and optimised MC-MPPA designs numerically and experimentally.

The remainder of this paper will be organised as follows: Section 2 describes the geometric design of the MC-MPPA; Section 3 introduces the methods used in the current study, including the traditional equivalent circuit model, the graph-theory-based method, the finite element model and the experimental test-setup. Section 4 provides an initial validation of the newly proposed, graph-theory-based predictive analytical method (TpIM) using data from the literature and finite element model (FEM). The TpIM at this point has not been optimised. Section 5 describes the optimisation process, allowing characteristic geometric parameters of the MC-MPPA to be varied to maximise the sound absorption in a frequency range for a particular depth. Section 6 completes the validation of both the proposed predictive analytical method and optimised MC-MPPA designs numerically and experimentally. Sections 7 and 8 present the discussions and conclusions of the current study, respectively.

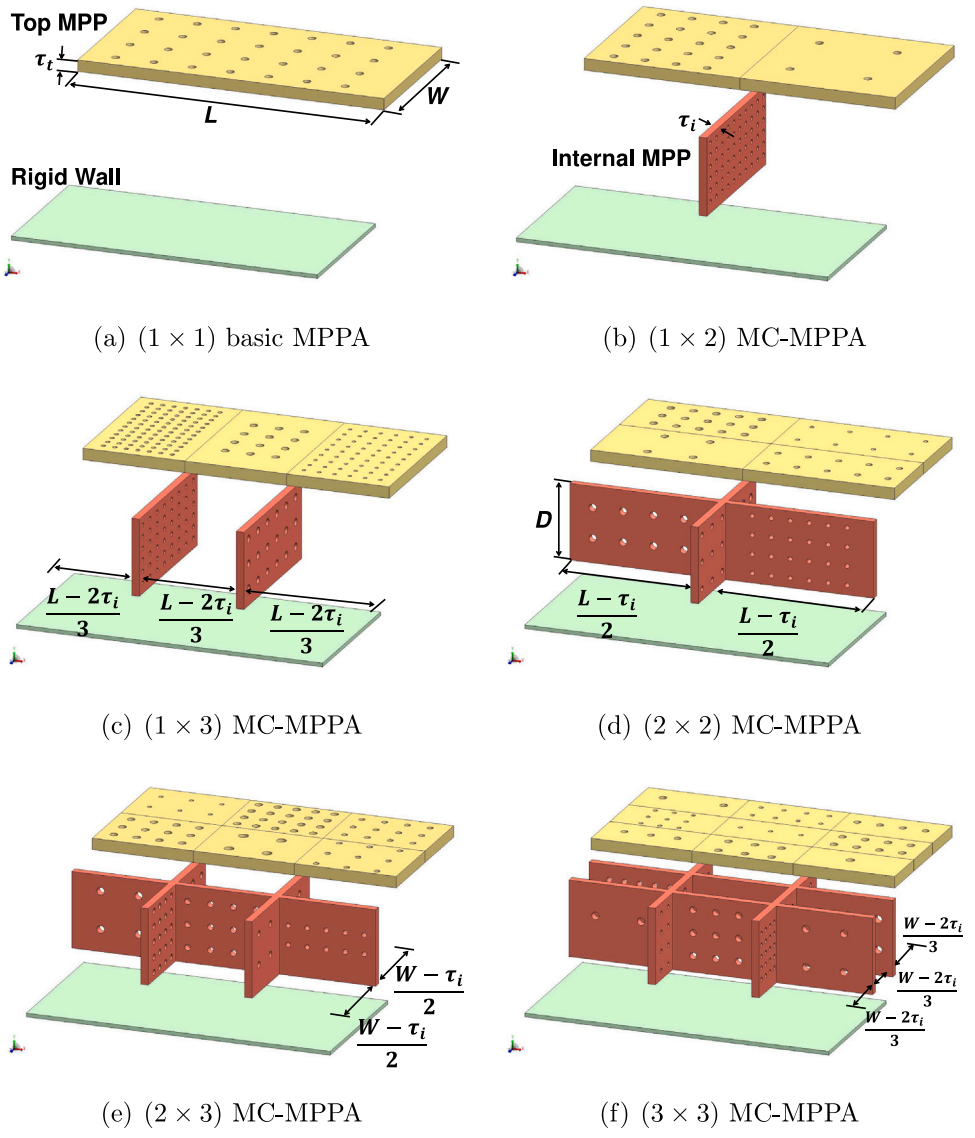

(a) (1 × 1) basic MPPA (b) (1 × 2) MC-MPPA

(c) (1 × 3) MC-MPPA (d) (2 × 2) MC-MPPA

(e) (2 × 3) MC-MPPA (f) (3 × 3) MC-MPPA

Fig. 1. Schematic representations of the MC-MPPAs examined. (For interpretation of the references to colour in this figure legend, the reader is referred to the web version of this article.)

2. Multi-chamber MPPA design

In this section, a rectangular MPPA with multi-chambers (MC-MPPA) is proposed, which is a complex acoustic system consisting of numerous micro-perforated panels (MPPs) and air cavities (ACs) (as shown in Fig. 1). This rectangular MPPA can be subdivided into M × N chambers where M and N are the numbers of chambers in the x-direction and y-direction, respectively.

Fig. 1 shows the geometric design of the (1 × 1), (1 × 2), (1 × 3), (2 × 2), (2 × 3) and (3 × 3) MC-MPPAs. One or more MPPs seal the top surface, and the remaining external surfaces of the MPPA are rigid unperforated panels. This paper refers to the top MPPs as $\mathrm{MPP}_{t(1,1)}$, $\mathrm{MPP}_{t(2,1)}$, ⋯, $\mathrm{MPP}_{t(M,N)}$, respectively. Each top MPP has an air-back cavity corresponding to it. These air cavities are referred to as $\mathrm{AC}_{(1,1)}$, $\mathrm{AC}_{(1,2)}$, ⋯, $\mathrm{AC}_{(\mathrm{M,N})}$, respectively. In the current study, each air cavity has the same depth, D.

Regardless of the number of chambers inside the MC-MPPA, the overall shape of the MC-MPPA is rectangular, allowing it to be easily tessellated for practical industrial applications. The overall length and width of the absorber is set to be L and W respectively. The height, H, of the MPPA is obtained by adding the thickness of the top MPP τ_t to the maximum depth, D, of the AC.

Inside the MPPA, adjoining chambers are separated by internal side-wall MPPs. We need to label each internal MPP with a number to facilitate their mathematical treatment in the optimisation process. However, since the identification of the internal MPP is more complex compared to the top MPPs, it cannot be simply labelled as $\mathrm{MPP}_{i(1,1)}$, $\mathrm{MPP}_{i(1,2)}$, ⋯, $\mathrm{MPP}_{i(N-1,M-1)}$, etc. Instead, we label internal MPPs as $\mathrm{MPP}_{i(1)}$, $\mathrm{MPP}_{i(2)}$, ⋯, $\mathrm{MPP}_{i((M-1)N+(N-1)M)}$, respectively using a serpentine naming method.

Table 1
Constitutive parameters of the MC-MPPAs under study.

Location of MPPs	Symbol of MPPs	Panel thickness	Perforation diameter	Perforation porosity	Perforation number
Top surface of MC-MPPA	$\mathrm{MPP}_{t(1,1)}$	τ_t	$d_{t(1,1)}$	$\varphi_{t(1,1)}$	$n_{t(1,1)}$
	$\mathrm{MPP}_{t(1,2)}$		$d_{t(1,2)}$	$\varphi_{t(1,2)}$	$n_{t(1,2)}$
	$\mathrm{MPP}_{t(1,3)}$		$d_{t(1,3)}$	$\varphi_{t(1,3)}$	$n_{t(1,3)}$
	⋮		⋮	⋮	⋮
	$\mathrm{MPP}_{t(M,N)}$		$d_{t(M,N)}$	$\varphi_{t(M,N)}$	$n_{t(M,N)}$
Internal walls of MC-MPPA	$\mathrm{MPP}_{i(1)}$	τ_i	$d_{i(1)}$	$\varphi_{i(1)}$	$n_{i(1)}$
	$\mathrm{MPP}_{i(2)}$		$d_{i(2)}$	$\varphi_{i(2)}$	$n_{i(2)}$
	$\mathrm{MPP}_{i(3)}$		$d_{i(3)}$	$\varphi_{i(3)}$	$n_{i(3)}$
	⋮		⋮	⋮	⋮
	$\mathrm{MPP}_{i((M-1)N+(N-1)M)}$		$d_{i((M-1)N+(N-1)M)}$	$\varphi_{i((M-1)N+(N-1)M)}$	$n_{i((M-1)N+(N-1)M)}$

Table 1 presents the constitutive parameters of the MC-MPPA under study with the four controlling parameters for MPPs defined as follows:

- panel thickness τ;
- perforation diameter d;
- perforation porosity φ (ratio of micro-perforated area to total area).
- perforation number n

It is worth noting that in this study, all the top MPPs have the same panel thickness, τ_t, as each other. Similarly, all the internal MPPs have the same panel thickness τ_i as each other, the value of which may be the same or different to that of τ_t. Allowing these parameters to vary relative to each other would certainly increase the capacity for optimisation but would significantly increase the complexity of manufacturing. In addition, if the top MPPs were to vary in thickness independently of the cavity depths the result would be an uneven surface which would cause difficulty in applications with flow [36–38].

The acoustic impedance Z_{mpp} of each MPP can be calculated by Eq. (1). In this paper, COMSOL's interior perforated thin panel boundary condition to calculate the MPP impedance [19,34] is used. In a previous numerical study [19], this has been shown to agree closely with fully resolved perforated holes in a COMSOL model.

$$\frac{Z_{\mathrm{mpp}}}{\rho_0 c_0} = -\left(\frac{\mathrm{i}\omega}{c_0\varphi}\frac{\tau + 8d\Lambda(\varphi)/3\pi}{Y_v}\right) \tag{1}$$

where i is the imaginary unit, ρ_0 is the air density and c_0 is the sound speed in air. The angular frequency is defined as $\omega = 2\pi f$ where f is the frequency in Hertz. The term Y_v is given by

$$Y_v = \frac{J_2\left(k_v d/2\right)}{J_0\left(k_v d/2\right)}, \quad k_v = \sqrt{-\frac{\mathrm{i}\omega\rho_0}{\mu}} \tag{2}$$

where J_n is the nth order Bessel function and μ is the dynamic viscosity of air.

The hole-to-hole interaction, if any, is determined by the Fok function, $\Lambda(\varphi)$, which is expressed by

$$\Lambda(\varphi) = \sum_{n=0}^{8} a_n(\sqrt{\varphi})^n \tag{3}$$

where the following first eight coefficients [19] are used in this study: $a_0 = 1$, $a_1 = -1.4092$, $a_2 = 0$, $a_3 = 0.33818$, $a_4 = 0$, $a_5 = 0.06793$, $a_6 = -0.02287$, $a_7 = 0.063015$ and $a_8 = -0.01614$.

Regarding the air cavities within the MPPA, the acoustic impedance, Z_{ac}, of each AC can be calculated by Eq. (4).

$$Z_{\mathrm{ac}} = -\mathrm{i}\rho_0 c_0 \cot\left(\frac{\omega D}{c}\right) \tag{4}$$

3. Methods

3.1. Equivalent circuit model (ECM) of an MC-MPPA

Analogies have been drawn between electronics and acoustics for many years which allow equivalent circuit models to be developed and for analysis and simplification methods to be transferred between the domains. Fig. 2 shows ECMs of the (1 × 2) and (1 × 3) chamber MC-MPPAs. The standard approach to obtain the impedance between the input and output terminals of these *planar* circuits is to follow a series of steps to simplify the circuit using $\Delta - Y$ transforms, for example.

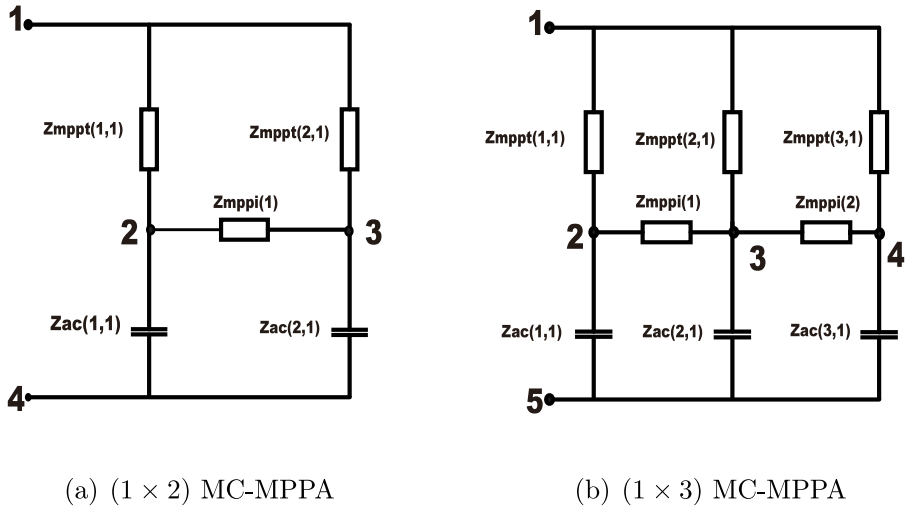

Fig. 2. MC-MPPA Equivalent circuit models.

As an illustration, the (1 × 2) chamber MPPA as seen in Fig. 2(a), can initially be simplified as

$$\begin{aligned} Z_A &= \frac{Z_{24}Z_{34}}{Z_{24}+Z_{34}+Z_{23}} \\ Z_B &= \frac{Z_{24}Z_{23}}{Z_{24}+Z_{34}+Z_{23}} \\ Z_C &= \frac{Z_{34}Z_{23}}{Z_{24}+Z_{34}+Z_{23}} \end{aligned} \tag{5}$$

where Z_{ij} in these equations is the acoustic impedance between nodes i and j. For more detail of the steps taken in this and the following simplification processes please refer to the work of Carbajo et al. [28] and McKay et al. [19]. Following this initial step, the acoustic impedance between nodes 1 and 4 in Fig. 2 (a) can be calculated to be

$$Z_{14} = \frac{\left(Z_{12}+Z_B\right)\left(Z_{13}+Z_C\right)}{Z_{12}+Z_{13}+Z_B+Z_c} + Z_A \tag{6}$$

Given this value, the specific impedance z_{14} is given by

$$z_{14} = Z_{14}S \tag{7}$$

where S is the area of normal incidence of the sound wave.

The reflection coefficient R, which is a function of the impedance, is given by the expression

$$R = \frac{z_{14}-\rho_0 c_0}{z_{14}+\rho_0 c_0} \tag{8}$$

and from this the normal incidence sound absorption coefficient α can be calculated according to

$$\alpha = 1 - |R|^2 \tag{9}$$

For the second example in Fig. 2, the (1 × 3) chamber MC-MPPA, the acoustic impedance between nodes 1 and 5 can be simplified to be

$$Z_{15} = \frac{\left(Z_{14}+Z_{C2}\right)\left(Z_A+Z_{A1}+Z_{B2}\right)}{Z_{14}+Z_{C2}+Z_A+Z_{A1}+Z_{B2}} + Z_{A2} \tag{10}$$

Details of the derivation of Eq. (10) can be found in Appendix A.

3.2. Two-point impedance method (TpIM) applied to the MC-MPPA

Fig. 3 shows the MC-MPPAs from Fig. 1 represented schematically as bi-pyramid molecular structures where the yellow branches represent the acoustic impedances of the top MPPs, the red branches represent the acoustic impedances of internal MPPs and the green branches represent the acoustic impedances of the air cavities themselves.

The two-point impedance method can be used to determine the impedance between any two nodes in a complex impedance network [35,39] whether the circuit is planar or not. Whilst the ECM methods in Section 3.1 are possible to apply to simple circuits,

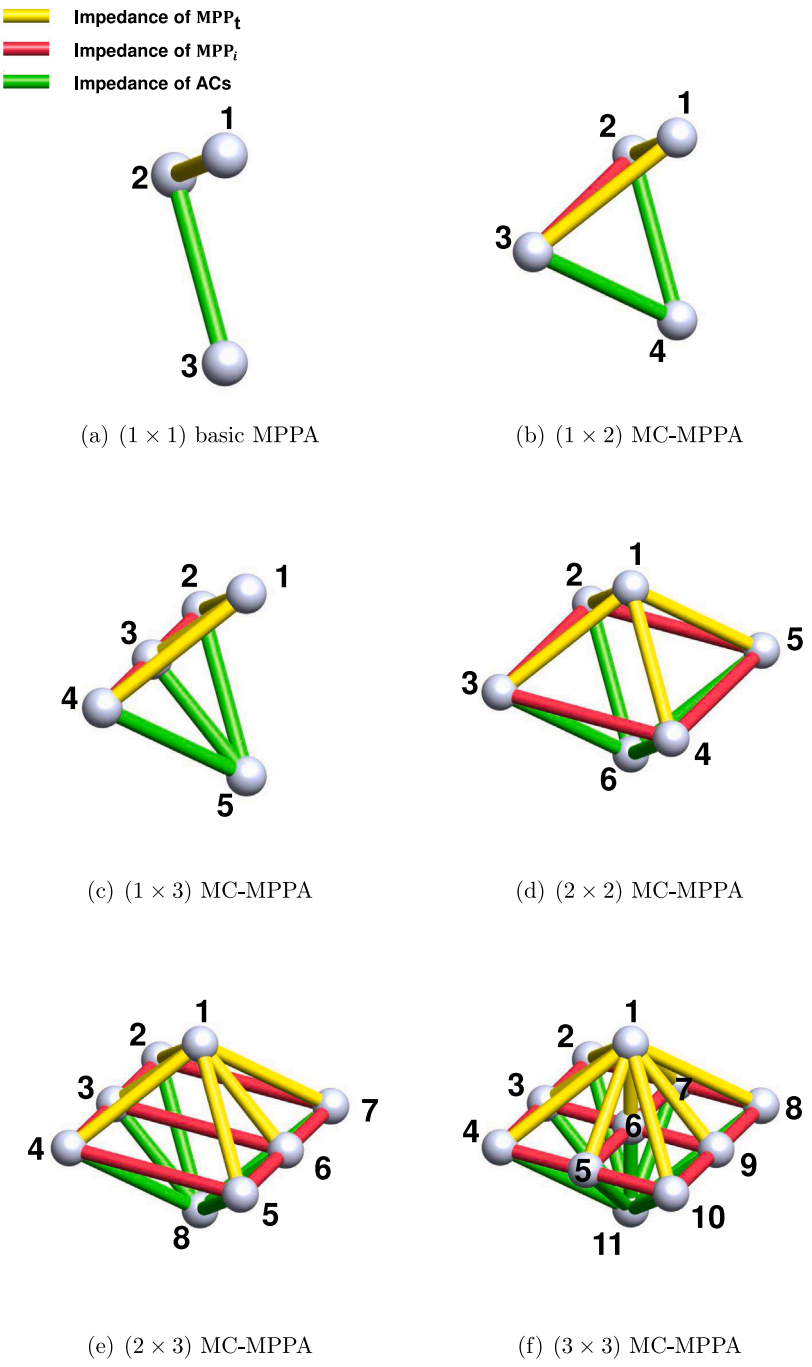

(a) (1×1) basic MPPA

(b) (1×2) MC-MPPA

(c) (1×3) MC-MPPA

(d) (2×2) MC-MPPA

(e) (2×3) MC-MPPA

(f) (3×3) MC-MPPA

Fig. 3. MC-MPPA molecular structures. (For interpretation of the references to colour in this figure legend, the reader is referred to the web version of this article.)

they become unmanageable for more complex non-planar circuits required by the higher order MC-MPPAs, some of which are illustrated in Figs. 3(d), (e) and (f).

Initially, the TpIM method was used in electrical engineering to analyse complex circuits. In the paper of Davis et al. [34], it was applied to determine the acoustic impedance between any two nodes of a complex acoustic system. In this paper, the two-point impedance method is presented to estimate the acoustic impedance of the multi-chamber MPPA complex acoustic system without the requirement of equivalent circuit simplification. The great advantage of the TpIM is that being matrix based, it makes the acoustic

Table 2
Details of FEM parameters settings.

Name	Value
Temperature	293.15 K
Air density	1.204 kg m^{-3}
Speed of sound	343.1 m s^{-1}
Air dynamic viscosity	1.825×10^{-5} kg (m s)$^{-1}$
Tube length	0.2 m

system intuitive. The TpIM is able to accurately estimate the impedance between any two nodes, regardless of the dimensionality of the circuit.

Based on this molecular structure, the following Laplace matrix $\mathbf{L}$ can be constructed:

$$\mathbf{L} = \begin{pmatrix} y_{11} & -y_{12} & \cdots & -y_{1\mathcal{N}} \\ -y_{21} & y_{22} & \cdots & -y_{2\mathcal{N}} \\ \vdots & \vdots & \ddots & \vdots \\ -y_{\mathcal{N}1} & -y_{\mathcal{N}2} & \cdots & y_{\mathcal{N}\mathcal{N}} \end{pmatrix} \tag{11}$$

where $\mathcal{N} = (\mathrm{M} \times \mathrm{N}) + 2$ is the number of nodes, y_{ij} is the admittance between nodes i and j, and $y_{ij} = y_{ji} = 1/Z_{ij}$ $(i \neq j)$, with Z_{ij} being the acoustic impedance between nodes i and j.

The diagonal elements of the Laplace matrix $\mathbf{L}$ can be given by

$$y_{ii} \equiv \sum_{j=1}^{\mathcal{N}} y_{ij} \quad i \neq j \tag{12}$$

Use of the Laplace matrix, $\mathbf{L}$, allows us to form the Hermitian matrix $\mathbf{L}^{\dagger}\mathbf{L}$, which can be diagonalised and where $\dagger$ denotes the hermitian conjugate. In order to calculate the impedance of the network represented by the Laplace matrix, the following eigenvalue equation must be solved:

$$\mathbf{L}^{\dagger}\mathbf{L}\psi_{\beta} = \eta_{\beta}\psi_{\beta}, \quad \eta_{\beta} \geqslant 0, \quad \beta = 1, 2, \ldots, \mathcal{N} \tag{13}$$

where η_{β} and ψ_{β} are the eigenvalues and eigenvectors of $\mathbf{L}^{\dagger}\mathbf{L}$ respectively. Then there exist eigenvalues of $\mathbf{L}$, which can be given by

$$\lambda_{\beta} = \psi_{\beta}^{\dagger}\mathbf{L}\psi_{\beta} \tag{14}$$

Finally, the acoustic impedance between any two nodes i and j in the network is given by

$$Z_{ij} = \sum_{\beta=2}^{\mathcal{N}} \frac{1}{\lambda_{\beta}} \left(\psi_{\beta}(i) - \psi_{\beta}(j)\right)^2 \tag{15}$$

Given this value, the specific impedance z_{ij} can be calculated from Eq. (7) and the normal incidence sound absorption coefficient, α, can be calculated from Eqs. (8) and (9).

Further detail and illustrations of how the TpIM can be used to simplify complex acoustic circuits can be found in Davis et al. [34].

3.3. Finite element model (FEM)

Initially, the ECM method will be used to validate the TpIM but this can only be done for some simple circuits. In addition, a finite element analysis using COMSOL Multiphysics 6.0. was conducted in order to validate both the TpIM and ECM results for simple circuits and the TpIM for more complex circuits. Both of these latter methods, once developed, are quick to execute which is to their benefit but they both depend on a lumped element assumption. As the objective of this research is to develop noise-absorbing technologies which are thin and for them to be efficient at low frequencies, this assumption should not be violated but it is still necessary to verify their accuracy. The complex and non-planar (2 × 3) MC-MPPA, as shown in Fig. 4, illustrates one of the test-set ups and the boundary conditions. As is standard, an impedance tube style set-up was implemented numerically with a normally incident plane wave pressure field being generated upstream of the test section. The pressure acoustics module was implemented to model the air domain both upstream and in the air cavities. For the MPPs, COMSOL's interior perforated thin panel boundary condition, Eq. (1), was implemented. In previous work by McKay et al. [19] for a similar set-up, it was demonstrated that the IPP boundary condition provides results as accurate as a fully resolved model of the holes themselves with much less computational cost. The detail of the global parameters used in the simulations are listed in Table 2.

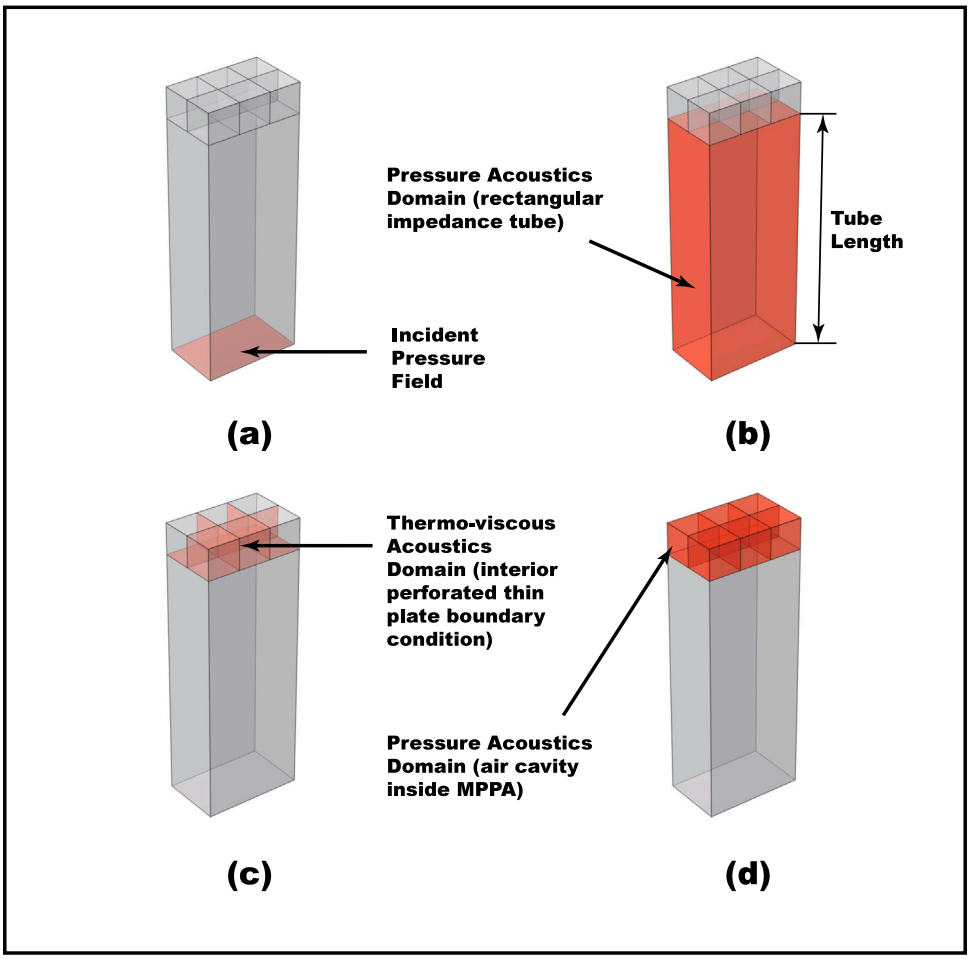

Fig. 4. COMSOL Multiphysics FEM model of (2 × 3) MC-MPPA.

3.4. Experimental setup

A rectangular impedance tube, as shown in Fig. 5, with internal cross-sectional dimensions of 80 mm × 50 mm was used to experimentally measure the normal acoustic incidence sound absorption coefficients of the MC-MPPAs. The experimental set-up is in accordance with the ISO 10534-2:1998 Standard [40]. The plane wave cut-off frequency of this experimental rig is approximately 2100 Hz. Two 150 W BMS 4591 2" compression drivers are placed at one end of the tube to generate planar sound waves and test samples are mounted to the other end. Due to the compression drivers' reduced low-frequency response, the lower frequency limit for sound absorption measurements using this experimental rig is 200 Hz, and thus, experimental results will be presented from above this low-frequency limit. The microphones used in the measurements were G.R.A.S 40PH microphones. The 40PH has a flat frequency response from 20 Hz to 20 kHz, in excess of the frequency range of the acoustic drivers and the analysis conducted.

The MC-MPPAs were 3D printed. Technologies such as these are difficult and expensive to manufacture using traditional fabrication techniques and it is due to the advances in 3D printing methods that such great strides have been possible in AMM development [41–44]. The additive manufacturing 3D printer used in this work was an Elegoo Saturn S masked stereolithography (mSLA) printer. Stereolithography is a form of additive manufacturing often used for fast prototyping, particularly when the prototype involves small features, and thus, is very suitable for the small micro-perforations of the MC-MPPA. It uses a liquid resin photopolymer that can be cured when exposed to UV light. The cured resin forms very thin solid layers which stack to form the object. Stereolithography is often used in prototyping as it is able to achieve high levels of precision and accuracy. The Elegoo Saturn S has a 9.1" LCD screen with a 48 μm xy resolution. It can print at layer heights from 0.01 mm up to 0.15 mm, and has a z-axis resolution of 1.25 μm.

In order to validate the performance experimentally of the MC-MPPA, it was compared to a single-layer of Basotect G+ (BASF, Germany) of the same dimensions. Basotect G+ is a melamine resin foam with a high sound absorption capacity and is an industry-standard [45]. The same impedance tube set-up was used to measure its absorption coefficient as a function of its thickness. Fig. 6

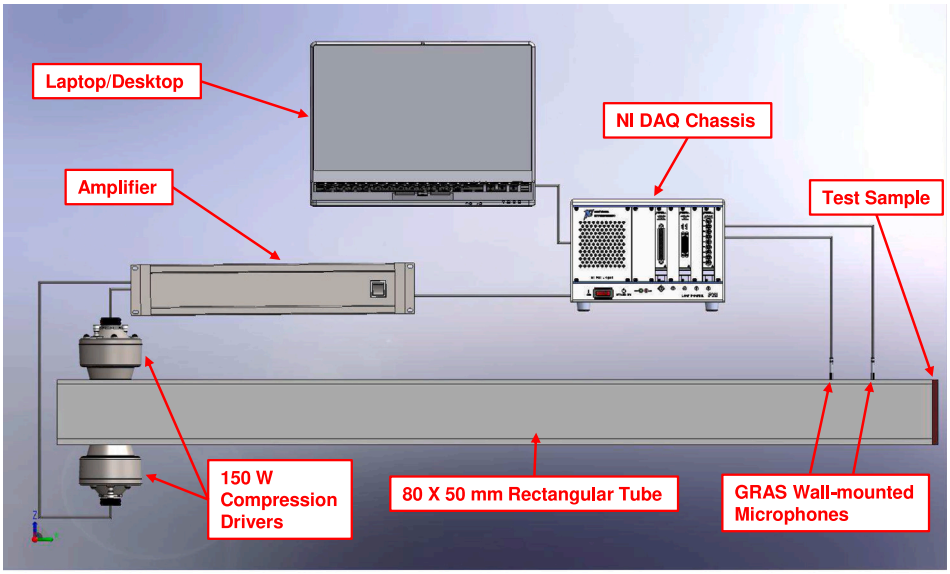

(a) Illustration of the rectangular impedance tube used to measure MC-MPPA's sound absorption coefficients

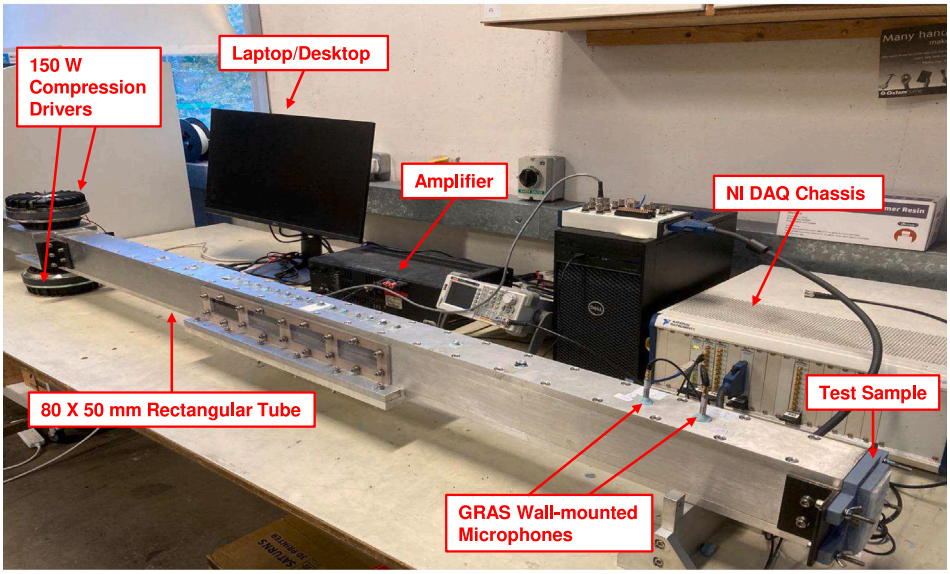

(b) Photo of this rectangular impedance tube

Fig. 5. Experimental rig test set-up.

shows the test set-up. The block of Basotect G+ was placed in a solid holder with a thick aluminium backing. A rubber gasket was placed between the holder and the aluminium impedance tube to ensure no air leakage.

4. Initial validation of the TpIM

In order to test the validity of the proposed TpIM approach, the sound absorption of the (1 × 2) and (1 × 3) MC-MPPAs from 10 Hz to 3000 Hz was examined using the three different methods (ECM, TpIM and FEM) described in Section 3. The geometrical parameters of the perforated panels studied can be found in Table 3. In addition, a comparison is also made with the results of Carbajo et al. [28] from the literature. WebPlotDigitizer [46] was used to obtain the data from the Carbajo reference.

Fig. 7(a) shows the results for the (1 × 2) MC-MPPA. The width and length were set to be 10 mm and the depth to be 20 mm in order to agree with the dimensions of the Carbajo et al. [28] set-up. Fig. 7(b) shows the results for a (1 × 3) MC-MPPA. In order

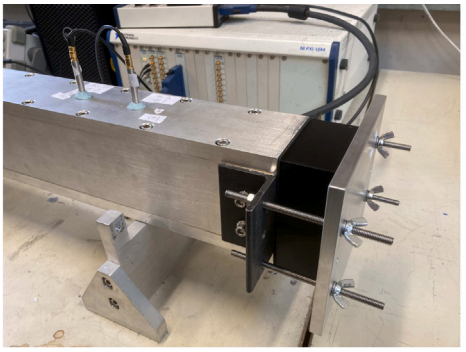

(a) Black sample holder with solid aluminium backing.

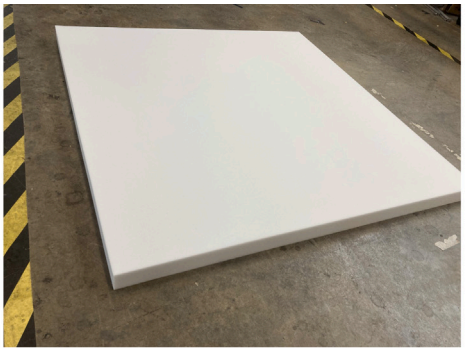

(b) Sample sheet of Basotect G+ melamine resin foam.

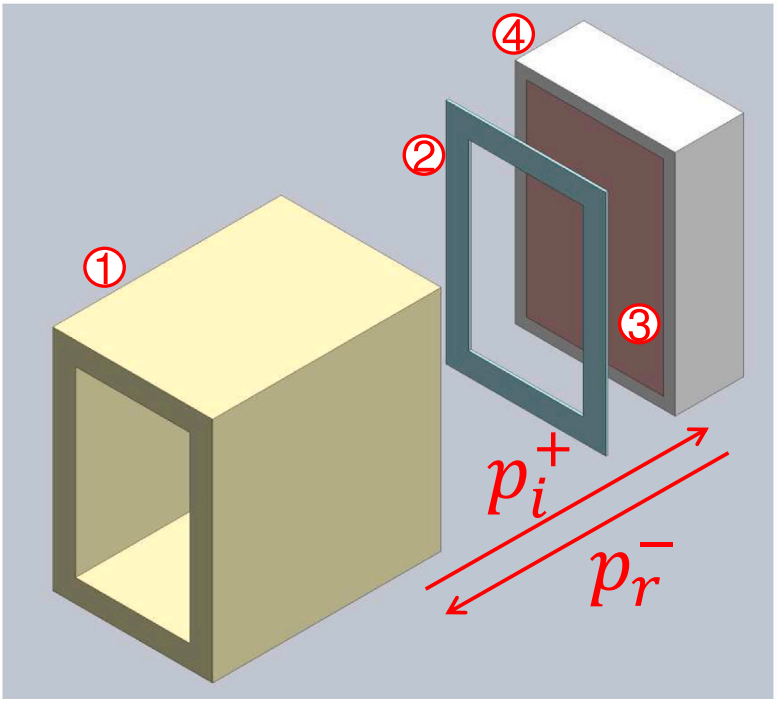

(c) 1: Impedance tube, 2: Rubber Gasket, 3: Block of Basotect G+, 4: Sample Holder.

Fig. 6. Experimental impedance tube test set-up for benchmarking against Basotect G+ melamine resin foam.

to investigate the performance with larger dimensions, the width, length and depth were chosen to be 40 mm, 40 mm and 25 mm respectively.

We see from both figures that the TpIM method produces the same results as the Kirchoff law-based ECM method, showing that this method can be used as an alternative approach complete with its advantages. We also see in both sets of figures that both models are validated by the finite element method of COMSOL. Finally, the results reproduced in this work for the (1 × 2) MC-MPPA agree perfectly with those published in the literature by Carbajo et al. [28].

Comparing the two figures from the point of view of performance, we see that both provide a high absorption coefficient close to unity with the frequency range of the deeper MC-MPPA decreasing, as would be expected, but with a narrower bandwidth.

5. Optimisation

The absorption coefficients of the MC-MPPAs in Fig. 7 are seen to be high for these relatively arbitrarily chosen parameters but the frequency responses are quite narrow, and typically become more so with decreasing frequency range. One of the main objectives

Table 3
Geometrical parameters of (1 × 2) and (1 × 3) MC-MPPAs as used in Section 4.

Type	Element	τ (mm)	d (mm)	φ (%)
1 × 2 chambers	$MPP_{i(1,1)}$	2	1	1
	$MPP_{i(2,1)}$	2	2	4
	$MPP_{i(1)}$	1	0.1	1
1 × 3 chambers	$MPP_{i(1,1)}$	2	1	1
	$MPP_{i(2,1)}$	2	1	1
	$MPP_{i(3,1)}$	2	1	1
	$MPP_{i(1)}$	1	0.1	0.8
	$MPP_{i(2)}$	1	0.1	0.8

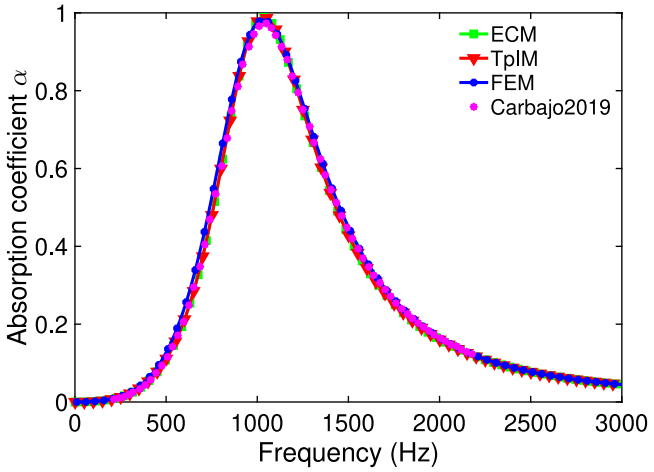

(a) (1 × 2) MC-MPPA

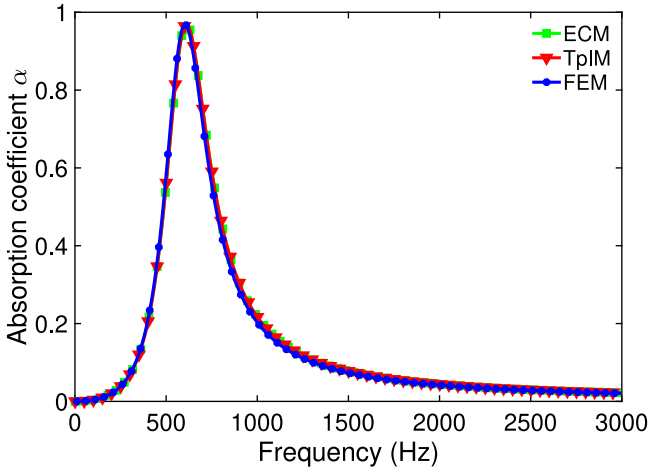

(b) (1 × 3) MC-MPPA

Fig. 7. Sound absorption coefficients.

of applying the TpIM to the MPPA technology is to provide an analytical model and with that model optimise the absorbers so that they are as efficient as they can be for a fixed set of parameters.

In the work of McKay et al. [19], the performance of the membrane-based acoustic absorber, SeMSA, was quantified by the linear averaging of the absorption coefficient spectrum in a defined frequency range to give an overall averaged absorption coefficient, $\bar{\alpha}$. However, this approach is really only suitable when the target noise spectrum to be absorbed is white. In this work, and in the work of Davis et al. [34], arbitrary target spectra, for example, those produced by industrial fans or aeroengines, which might contain a mixture of tones and broadband noise, are also of interest.

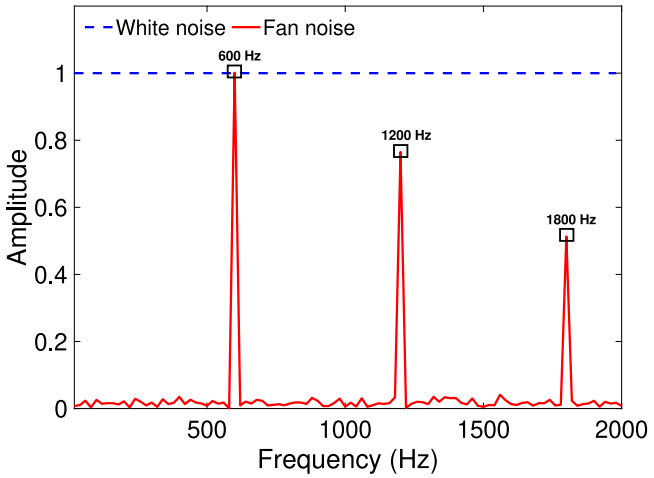

Fig. 8. Targeted sound spectra.

Considering a target sound spectrum described by an auto-spectral density function $G_{xx}(\omega)$, the sound power reduction that a sound absorber with an absorption spectrum $\alpha(\omega)$ would achieve in Decibels can be written as:

$$C_\alpha = 10log10(1 - c_\alpha) \tag{16}$$

where c_α is the overall absorption coefficient weighted by the sound spectrum of the targeted noise source:

$$c_\alpha = \frac{\left(\sum_{\omega_1}^{\omega_2} \alpha(\omega) G_{xx}(\omega)\right)}{\left(\sum_{\omega_1}^{\omega_2} G_{xx}(\omega)\right)} \tag{17}$$

and where $\omega_1 = 2\pi f_1$ and $\omega_2 = 2\pi f_2$, with f_1 and f_2 being the lower and upper limits of the frequency range of interest. The absorption coefficient, $\alpha(\omega)$, is calculated from Eq. (9) using the TpIM.

In the current study, to examine the potential optimal performance of the MC-MPPA, two target sound sources, $G_{xx}(\omega)$, are defined. Fig. 8 shows their sound spectra. For white noise, $G_{xx}(\omega) \equiv 1$, whereas the fan noise signal used here, simulated by Matlab, contains a fundamental tone plus two harmonics: with peaks at 600 Hz, 1200 Hz and 1800 Hz respectively.

The sound power reduction factor, C_α, provides a suitable cost function that can be minimised in an optimisation routine in order to generate the parameter set for an optimal MC-MPPA. C_α can be expressed as a function of the geometric parameter set chosen for the optimisation algorithm.

An optimisation method based on Sequential Quadratic Programming (SQP) was used to minimise the cost function. SQP is a classical iterative method for constrained nonlinear optimisation which applies to optimisation issues where the objective function and the constraints are twice continuously divisible. For more detail about SQP, we refer the readers to Refs. [47,48].

Here, we use Matlab's built-in fmincon SQP algorithm to complete the optimisation:

$$\begin{aligned} &\text{Minimise} \quad C_\alpha \quad \text{in} \quad \text{Eq.(16)} \\ &\text{subject to} \begin{cases} d_t(m,n) & \in [d_{\min} \quad d_{\max}], & m = 1,2,\cdot\cdot,\mathrm{M}; n = 1,2,\cdot\cdot,\mathrm{N} \\ d_i(j) & \in [d_{\min} \quad d_{\max}], & j = 1,2,\cdot\cdot,(\mathrm{M}-1)\mathrm{N} + (\mathrm{N}-1)\mathrm{M} \\ \varphi_t(m,n) & \in [\varphi_{\min} \quad \varphi_{\max}], & m = 1,2,\cdot\cdot,\mathrm{M}; n = 1,2,\cdot\cdot,\mathrm{N} \\ \varphi_i(j) & \in [\varphi_{\min} \quad \varphi_{\max}], & j = 1,2,\cdot\cdot,(\mathrm{M}-1)\mathrm{N} + (\mathrm{N}-1)\mathrm{M} \end{cases} \end{aligned} \tag{18}$$

Algorithm (18) does not apply to the basic (1 × 1) chamber MPPA which has no internal perforated sidewalls and so is treated more simply as:

$$\begin{aligned} &\text{Minimise} \quad C_\alpha \quad \text{in} \quad \text{Eq.(16)} \\ &\text{subject to} \begin{cases} d_t(m,n) & \in [d_{\min} \quad d_{\max}], & m = 1,2,\cdot\cdot,\mathrm{M}; n = 1,2,\cdot\cdot,\mathrm{N} \\ \varphi_t(m,n) & \in [\varphi_{\min} \quad \varphi_{\max}], & m = 1,2,\cdot\cdot,\mathrm{M}; n = 1,2,\cdot\cdot,\mathrm{N} \end{cases} \end{aligned} \tag{19}$$

The parameter settings for the optimisation are listed in Table 4. The flowchart for optimisation is shown in Fig. 9. To ensure that the optimisation results obtained are global rather than local, the following steps are taken:

Step 1 Input the absorber's length L, width W, air cavity depth D, top MPPs thickness τ_t and the internal sidewall MPPs thickness τ_i.

Table 4
Parameter settings for optimisation. Two ranges of hole diameters were examined.

Parameters	Value
$[d_{\min} d_{\max}]$	[0.05–0.3] mm, [0.3–1] mm
$[\varphi_{\min} \varphi_{\max}]$	[0–20]%
$[D_{\min} D_{\max}]$	[10–40] mm
$[f_1 f_2]$	[20–2000] Hz
$[L, W]$	[50 mm, 40 mm]
$[\tau_t, \tau_i]$	[2 mm, 1 mm]

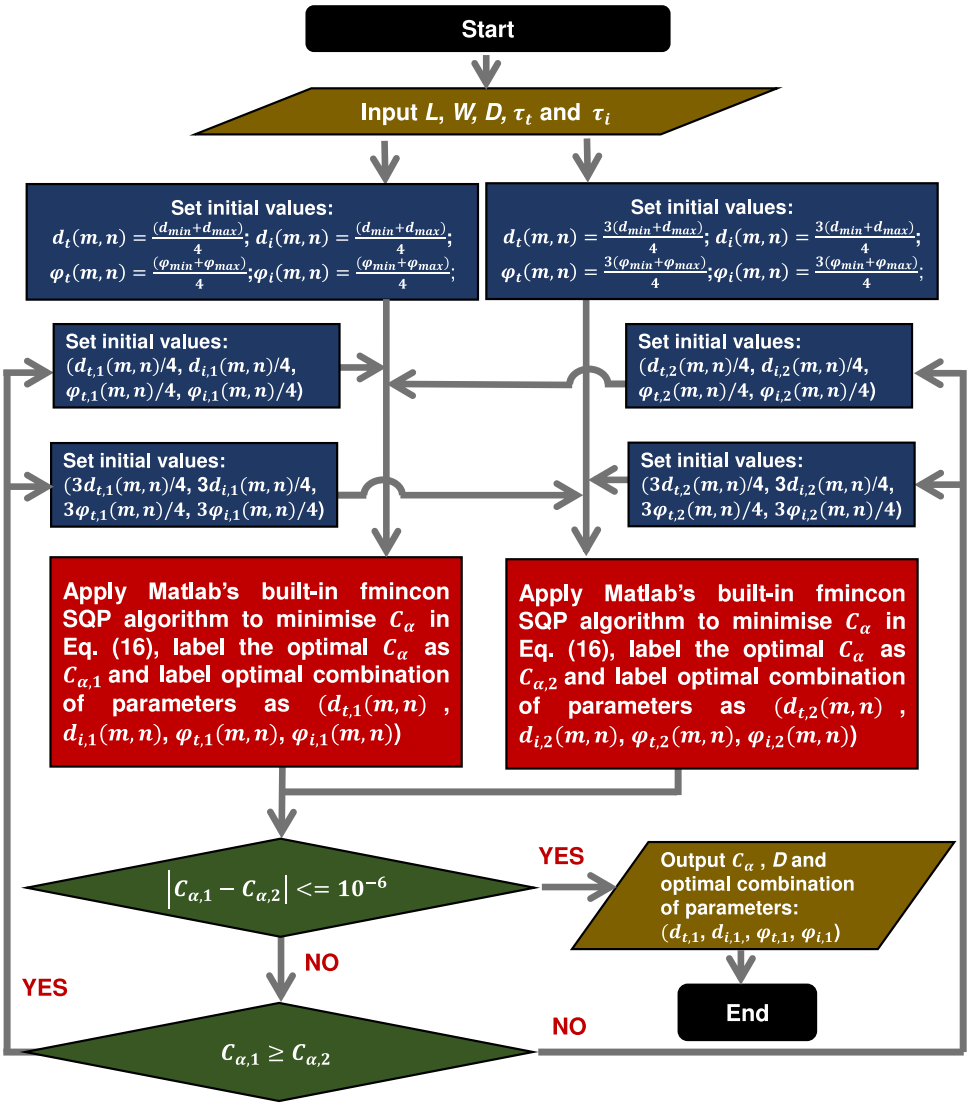

Fig. 9. Flowchart for optimisation.

Step 2 Two different initialisations are performed.

- One set of initial values are: $d_t(m,n) = \frac{(d_{\min}+d_{\max})}{4}$, $d_i(m,n) = \frac{(d_{\min}+d_{\max})}{4}$, $\varphi_t(m,n) = \frac{(\varphi_{\min}+\varphi_{\max})}{4}$, $\varphi_i(m,n) = \frac{(\varphi_{\min}+\varphi_{\max})}{4}$.
- After one round of optimisation with these initial values, the optimised results are labelled $C_{\alpha,1}$, $(d_{t,1}(m,n)$, $d_{i,1}(m,n)$, $\varphi_{t,1}(m,n)$ and $\varphi_{i,1}(m,n))$.
- The second set of initial values are: $d_t(m,n) = \frac{3(d_{\min}+d_{\max})}{4}$, $d_i(m,n) = \frac{3(d_{\min}+d_{\max})}{4}$, $\varphi_t(m,n) = \frac{3(\varphi_{\min}+\varphi_{\max})}{4}$, $\varphi_i(m,n) = \frac{3(\varphi_{\min}+\varphi_{\max})}{4}$.

– After one round of optimisation with this second set of initial values, the optimised results are labelled $C_{\alpha,2}$, ($d_{t,2}(m,n)$, $d_{i,2}(m,n)$, $\varphi_{t,2}(m,n)$, $\varphi_{i,2}(m,n)$).

Step 3 Optimisation results for the two different initialisation are compared.

– If $|C_{\alpha,1} - C_{\alpha,2} \leq 10^{-6}|$, we consider that the result is already a global optimal solution.
– If $|C_{\alpha,1} - C_{\alpha,2} > 10^{-6}|$, additional rounds of optimisation are required. Step 2 will be repeated, but the initialisation parameters will be changed as follows:
– If $C_{\alpha,1} \geq C_{\alpha,2}$, one set of initial values will be changed to: ($\frac{d_{t,1}(m,n)}{4}$, $\frac{d_{i,1}(m,n)}{4}$, $\frac{\varphi_{t,1}(m,n)}{4}$, $\frac{\varphi_{i,1}(m,n)}{4}$), the other set of initial values will be changed to: ($\frac{3d_{t,1}(m,n)}{4}$, $\frac{3d_{i,1}(m,n)}{4}$, $\frac{3\varphi_{t,1}(m,n)}{4}$, $\frac{3\varphi_{i,1}(m,n)}{4}$).
– If $C_{\alpha,1} < C_{\alpha,2}$, one set of initial values will be changed to: ($\frac{d_{t,2}(m,n)}{4}$, $\frac{d_{i,2}(m,n)}{4}$, $\frac{\varphi_{t,2}(m,n)}{4}$, $\frac{\varphi_{i,2}(m,n)}{4}$), the other set of initial values will be changed to: ($\frac{3d_{t,2}(m,n)}{4}$, $\frac{3d_{i,2}(m,n)}{4}$, $\frac{3\varphi_{t,2}(m,n)}{4}$, $\frac{3\varphi_{i,2}(m,n)}{4}$).

Step 4 As shown in Fig. 9, Steps 2 and 3 will be repeated over and over until the stopping criteria is met.

6. Results

In order to evaluate the performance of the MC-MPPA, four test cases were examined:

- Case 1. Target spectrum: White noise; Perforation diameter range: [0.05–0.3] mm.
- Case 2. Target spectrum: White noise; Perforation diameter range: [0.3–1.0] mm.
- Case 3. Target spectrum: Fan noise; Perforation diameter range: [0.05–0.3] mm.
- Case 4. Target spectrum: Fan noise; Perforation diameter range: [0.3–1.0] mm.

As has been discussed already, we want to assess how well the multi-chamber MPPA will absorb sound, and also how well the optimisation algorithm will perform, depending on the type of noise source present. Therefore, both white noise and tonal noise have been examined.

Further, a 0.3 mm perforation is approximately the smallest hole than can be reliably 3D printed in large numbers by a desktop 3D printer currently and is also about the size of the smallest drill bit that good workshops would be able to use in a CNC milling machine with thin panels. Therefore, we have examined two hole size ranges, each of which are the hole size ranges used in the optimisation routine. The [0.3 - 1] mm range is a manageable sub-millimetre range whether using 3D printing or traditional fabrication methods, whereas the [0.05–0.3] mm range examines towards the micron level with 0.05 mm (50 micron) being a common lower level examined in numerical studies of MPPAs to be found in the literature.

The absorption coefficient as a function of frequency, where the frequency range is from 20 Hz to 2 kHz, is plotted for each of the four cases in Figs. 10–13. To evaluate the impact of increasing the number of chambers in one and two dimensions and to compare them to the standard single chamber resonator, each of the six chamber configurations, as illustrated in Fig. 1, are examined.

Figs. 14–17 plot the overall absorption coefficients of Cases 1–4 and Basotect G+ in the frequency range from 200 Hz to 2000 Hz, weighted by the sound spectrum of the target source from Eq. (17). As previously discussed, the optimised analytical frequency range chosen for the MC-MPPAs was [20 2000] Hz. However, in Figs. 14–17 the [200 2000] Hz range is chosen to allow for comparison with the experimental results of the Basotech G+ benchmarking porous material. It should also be noted that the thickness of the air cavity of the MC-MPPAs is increased from 10 mm to 40 mm in 5 mm increments, and as the thickness of the MC-MPPAs' top MPP is 2 mm, the overall thickness of the MC-MPPAs is actually increased from 12 mm to 42 mm in 5 mm increments.

The specific values of c_α in the [200 2000] Hz frequency range, corresponding to Figs. 14–17 can be found in Appendix B.

6.1. Numerical validation

A second series of numerical simulations were carried out to prove the validity of the two-point impedance method. After having shown that the TpIM approach can provide equivalent results to the ECM method, now the *optimised* TpIM results are examined and also for the full test set of chambers from Fig. 1. Case 1 is chosen for the numerical validation, where white noise is chosen as the target spectrum and a very shallow depth of only 25 mm is examined to test the efficacy of the technology. Results are found in Figs. 18.

6.2. Experimental validation

Two (3 × 3) MC-MPPA test samples, named Test sample 50 and Test sample 20 respectively, were fabricated using an mSLA 3D-printing process using 405 nm Photopolymer Resin (colour: grey):

(1) **Test sample 50** (as shown in Fig. 19). Target spectrum: White noise; Perforation diameter range: [0.5–1.0] mm; Perforation porosity range: [0-5] %; Working frequency range: [200 1000] Hz and air cavity depth: 50 mm.
(2) **Test sample 20** (as shown in Fig. 20). Target spectrum: White noise; Perforation diameter range: [0.5–1.0] mm; Perforation porosity range: [0-5] %; Working frequency range: [200 2000] Hz and air cavity depth: 20 mm.

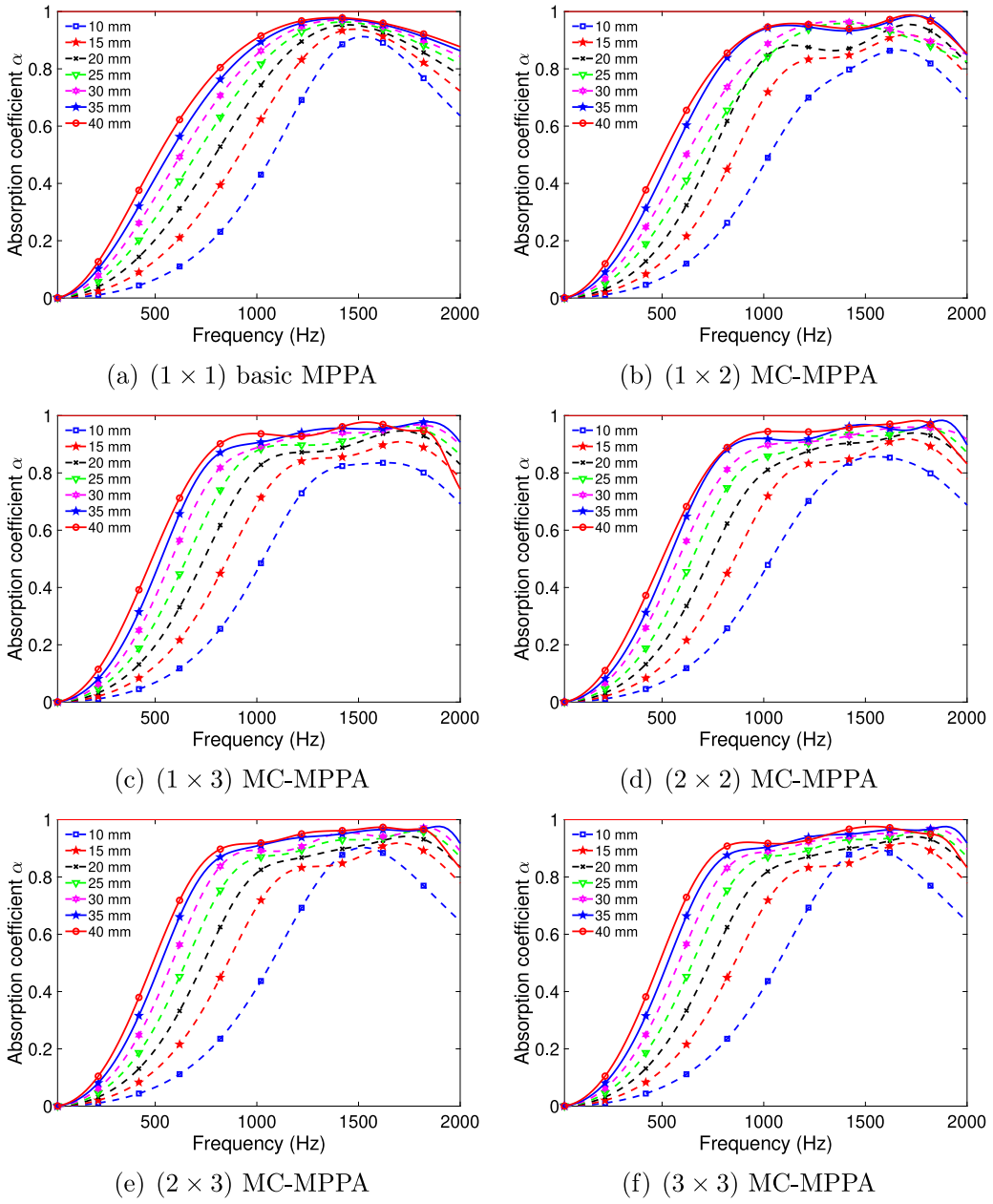

Fig. 10. Sound absorption coefficients for Case 1, air cavity depth range: [10 40] mm, frequency range: [20 2000] Hz, target spectrum: white noise and perforation diameter range: [0.05 0.3] mm, L = 50 mm, W = 40 mm.

Figs. 19 and 20 show CAD images and photos of the two experimental samples. Two depths were chosen for these samples. 50 mm (2") is a typical depth for an aeroengine acoustic liner in industry and 20 mm was chosen to test the abilities of this technology at a very small depth. The porosity range was decreased in order to reduce the optimum number of holes to reasonable quantities and, as with the Basotect analysis, the samples were optimised for frequencies above 200 Hz due to low-frequency limitations in the test rig. The full set of geometric parameters of these test samples can be found in Appendix C.

The Dino-Lite Premier AD7013MT digital desk-top microscope was used to assess the printing accuracy of the 3D-printed holes. Fig. 21 shows images taken by a microscope of four randomly selected 0.5 mm-diameter holes from test samples. Fig. 22 shows images taken by a microscope of four randomly selected 0.9 mm-diameter holes from test samples. For these samples, the averages for the diameters are 0.44 mm and 0.86 mm both of which are less than as designed. Kennedy et al. [49] discuss how deviations in surface roughness and dimensional fidelity can have a comparable impact on the experimentally measured values of the absorption coefficient. In further tests, it may be possible to calibrate the actual hole diameter printed to that designed.

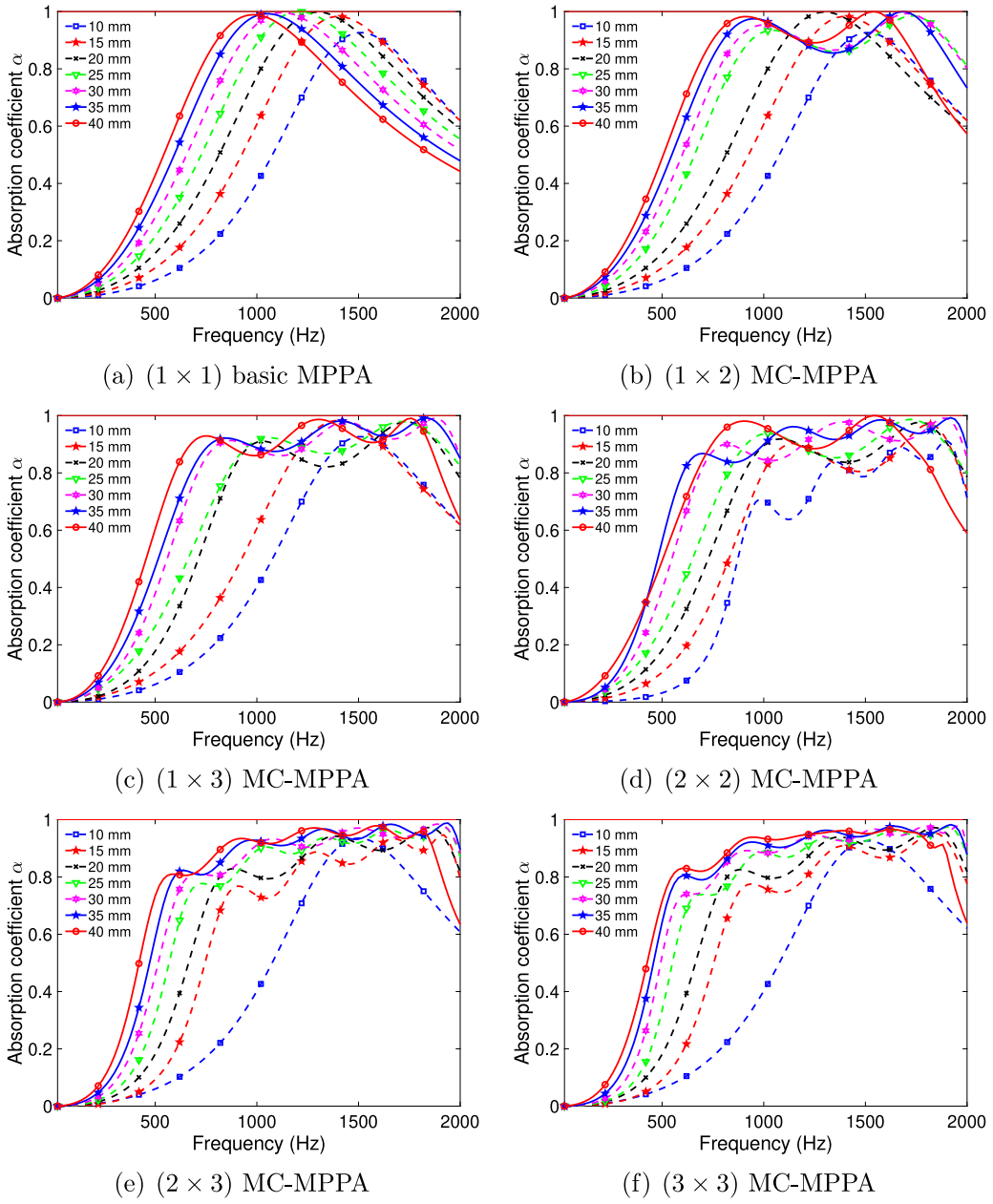

Fig. 11. Sound absorption coefficients for Case 2, air cavity depth range: [10 40] mm, frequency range: [20 2000] Hz, target spectrum: white noise and perforation diameter range: [0.3 1.0] mm, L = 50 mm, W = 40 mm.

The experimentally measured sound absorption curves for Test sample 50 and Test sample 20, and for the identically sized Basotect G+, are shown in Figs. 23 and 24.

7. Discussion

In order to understand the effects of the different parameters they are each examined in turn.

- **The effect of optimisation**
  A general observation can be made initially by comparing the spectra in Fig. 7 to those in Figs. 10 and 11. The spectral shapes for MPPAs as commonly seen in the literature are similar to those in Fig. 7, i.e. relatively narrowband with a bandwidth which decreases with frequency. However, while different parameters and configurations have been examined by researchers with

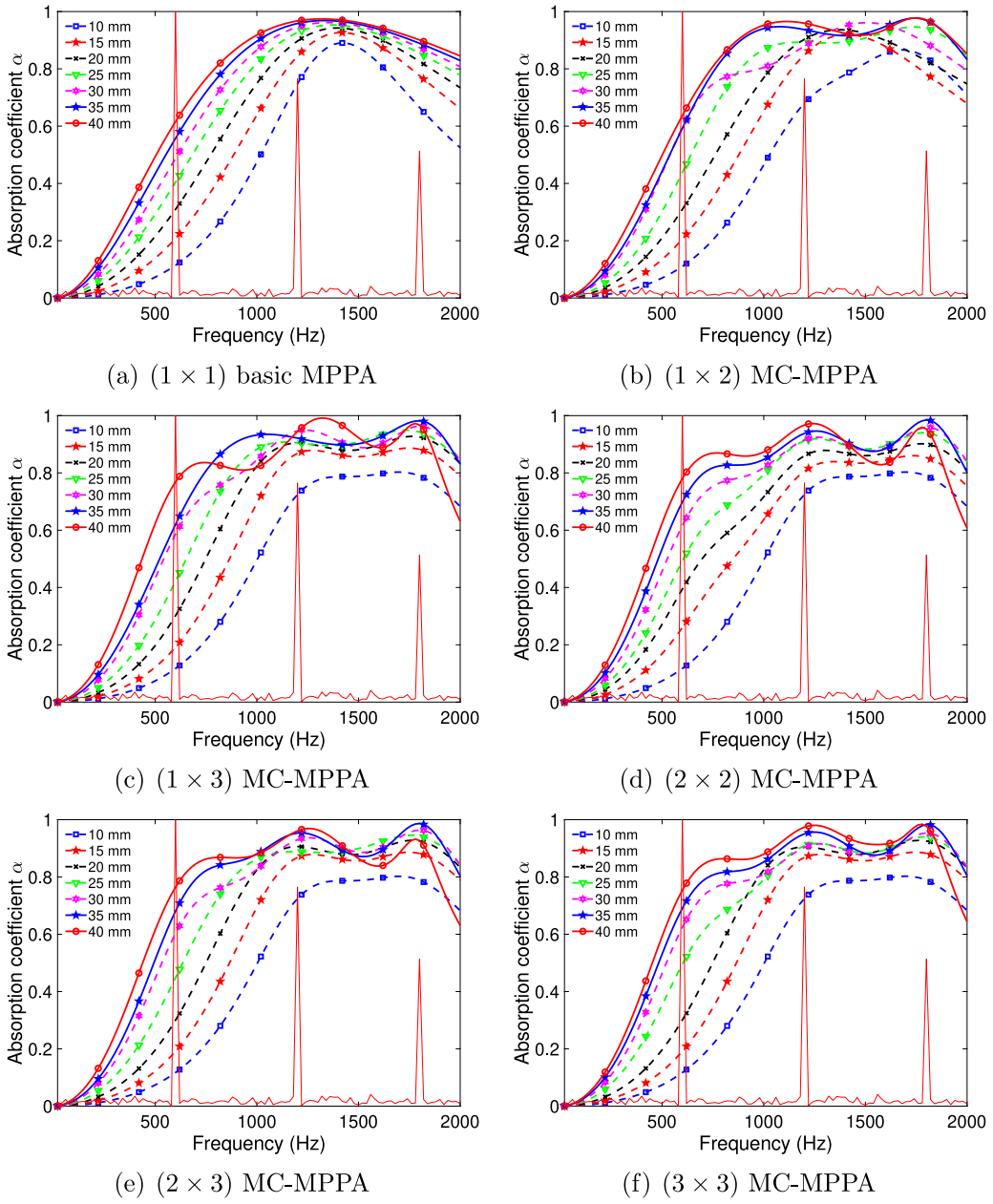

Fig. 12. Sound absorption coefficients for Case 3, air cavity depth range: [10 40] mm, frequency range: [20 2000] Hz, Target spectrum: fan noise and perforation diameter range: [0.05 0.3] mm, L = 50 mm, W = 40 mm.

a view to improving the absorption at the maximum peak or the effective frequency range, for example, there has been little optimisation conducted. It is clearly seen here that the capacity of the MPPA is significant once the parameters are optimised, with very significant gains to be made in bandwidth and magnitude upon a judicious choice of parameters. This applies to both the basic MPPA, as can be seen in Fig. 10(a), as well as to the MC-MPPA technology. Indeed, the application of optimisation to even the basic MPPA, resulting in greater bandwidth, is in itself a significant outcome of this work. Referring to Appendix B, we can see that the maximum overall absorption coefficient for the basic MPPA, for a thickness of 42 mm, is 0.79 in the 200 Hz - 2 kHz frequency range. In addition, at this same depth, all of the optimised MC-MPPAs have an absorption value greater than this, up to a maximum value of 0.91 for Case 4, making the TpIM optimisation process an extremely effective tool in absorber design.

- **The effect of perforation size**

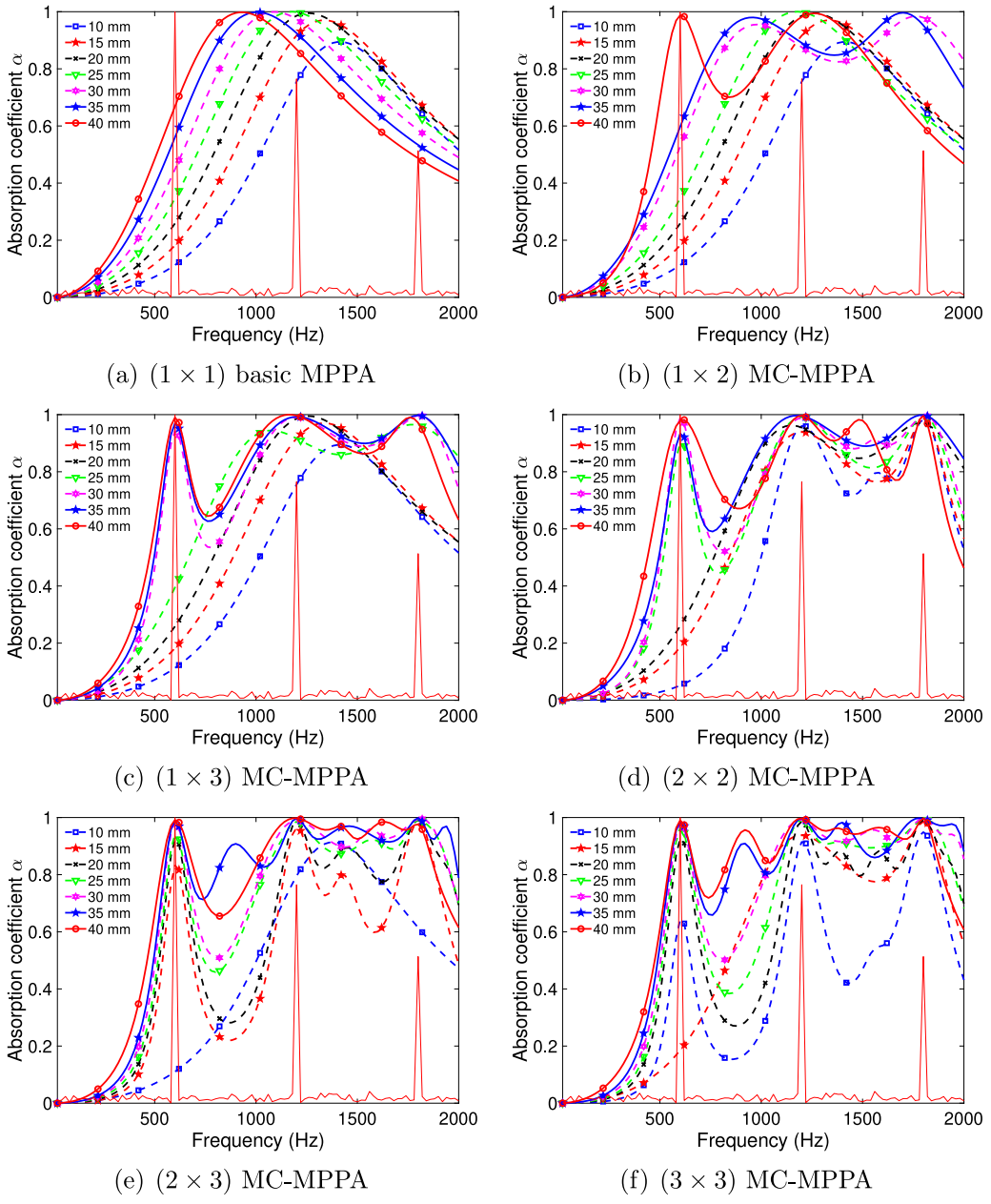

Fig. 13. Sound absorption coefficients for Case 4, air cavity depth range: [10 40] mm, frequency range: [20 2000] Hz, Target spectrum: fan noise and perforation diameter range: [0.3 1] mm, $L = 50$ mm, $W = 40$ mm.

White Noise Source. When the target sound source is white noise, a comparison between Case 1 (as shown in Fig. 10) and Case 2 (as shown in Fig. 11) as well as the values in Appendix B can be made to highlight the effect of pore diameter. Focusing initially on the (1 × 1) basic MPPA, for the larger hole diameter range (Case 2), the bandwidth is larger compared to that seen in Fig. 7, which has arbitrary values as opposed to optimised ones, and its maximum absorption coefficient is close to unity. As is typical with increasing depth, the frequency of the peak decreases. In addition, it is interesting to note that the overall absorption coefficient, c_α, actually increases somewhat from 0.48 at 12 mm absorber thickness to 0.65 at 42 mm absorber thickness. The behaviour in Case 1 for the basic MPPA with the smaller hole diameter range is somewhat different. With increasing depth, the magnitude tends towards unity and its bandwidth significantly increases in both frequency directions with the c_α values increasing from 0.48 for the 12 mm absorber thickness to 0.77 for the 42 mm absorber thickness. The increase in bandwidth with decreasing pore size is in agreement with the theory of Maa [2].

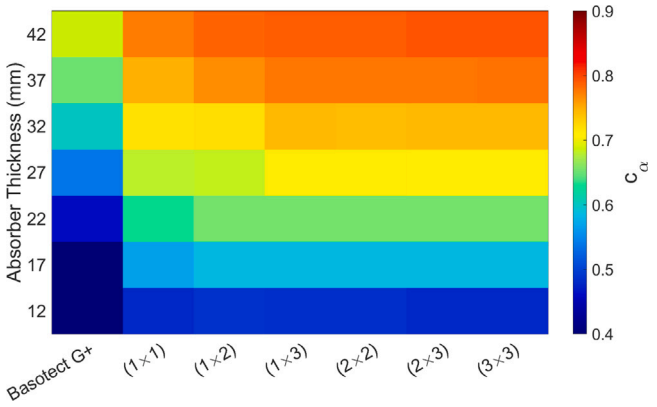

Fig. 14. Colourmap for Case 1 and Basotect G+ of overall sound absorption coefficient c_a, overall thickness [12 42] mm, frequency range: [200 2000] Hz. Numerical values can be found in Appendix B. (For interpretation of the references to colour in this figure legend, the reader is referred to the web version of this article.)

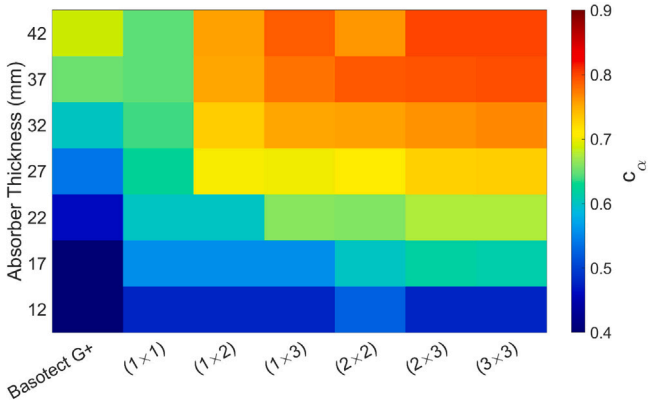

Fig. 15. Colourmap for Case 2 and Basotect G+ of overall sound absorption coefficient c_a, overall thickness [12 42] mm, frequency range: [200 2000] Hz. Numerical values can be found in Appendix B. (For interpretation of the references to colour in this figure legend, the reader is referred to the web version of this article.)

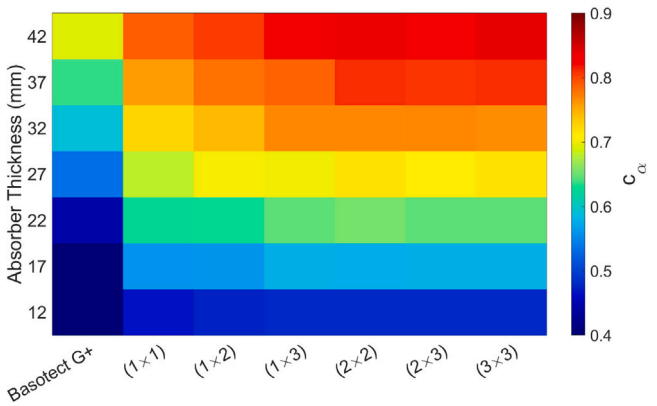

Fig. 16. Colourmap for Case 3 and Basotect G+ of overall sound absorption coefficient c_a, overall thickness [12 42] mm, frequency range: [200 2000] Hz. Numerical values can be found in Appendix B. (For interpretation of the references to colour in this figure legend, the reader is referred to the web version of this article.)

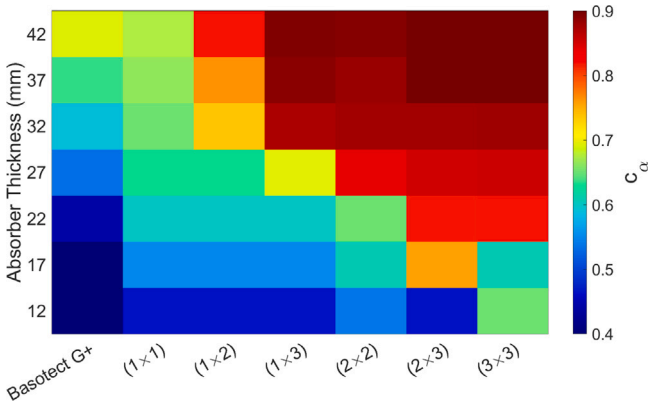

Fig. 17. Colourmap for Case 4 and Basotect G+ of overall sound absorption coefficient c_α, overall thickness [12 42] mm, frequency range: [200 2000] Hz. Numerical values can be found in Appendix B. (For interpretation of the references to colour in this figure legend, the reader is referred to the web version of this article.)

For the MC-MPPAs, the main difference due to the pore size range is that, interestingly, the larger pore size range is advantageous, as it allows the lower frequency tone to be attenuated.

For the MC-MPPAs, from observation of Case 2, we see that the absorption curves contain a number of perturbations in magnitude as a function of frequency which seem to be related to the number of chambers. These perturbations, however, seem to be damped by the smaller pore diameters of Case 1. The other key difference is that for the higher pore diameter range, lower frequencies can be attenuated.

Fan Noise Source. When the target sound source is fan noise as opposed to white noise, a comparison between Case 3 (as shown in Fig. 12) and Case 4 (as shown in Fig. 13), as well as the values in Appendix B, can be made to highlight the effect of pore diameter.

For the (1 × 1) basic MPPA, the behaviour and values are almost unchanged between the white noise and fan noise cases i.e. Fig. 12(a) vs Fig. 10(a) and Fig. 13(a) vs Fig. 11(a). This indicates that there is no scope for the optimisation algorithm to target the attenuation of tones when the technology is the basic MPPA.

In contrast with the (1 × 1) basic MPPA, referring now to the multi-chamber MPPAs, the behaviour between the small and large pore diameter range for the fan source is quite different. With increasing depth and chamber number, the smaller pore diameter range MC-MPPAs are able to form 2–3 peaks, the higher frequency two performing excellently at matching the frequency of the associated tones, whereas, the lower frequency peak in the absorption curve is unable to descend to the fundamental frequency to mask it fully.

For the larger pore diameter range, however, all tones can be frequency matched successfully, the more so with increasing depth and chamber number.

- **The effect of multiple chambers**

  Referring to Appendix B, and paying attention to the numbers in bold, we see that the value of the overall absorption coefficient, c_α, increases in value with an increasing number of chambers with the (3 × 3) MC-MPPA generally performing best with c_α values of between 0.79 and 0.91 for the (3 × 3) MC-MPPA at 42 mm absorber thickness versus 0.65 and 0.79 for the (1 × 1) basic MPPA.

  Referring to the frequency plot of Fig. 11, we see that by increasing the number of chambers and the air cavity depth, the response approaches a square wave with high amplitude absorption spreading over an increasingly broad frequency range.

  Referring to the frequency plot of Fig. 13, we see that by increasing the number of chambers, the absorption response is ever more capable of masking the tonal peaks in addition to filling the intervals with increasing air cavity depth.

  Finally, by referring to Figs. 14–17, it is particularly stark how the MC-MPPAs perform better than the (1 × 1) basic MPPA with regards to c_α value for the larger pore diameter range, i.e. Figs. 15 and 17, whereas whilst the MC-MPPAs are also significantly better than the (1 × 1) basic MPPA for the smaller pore diameter range, the improvement is not quite as great.

- **Comparison with the benchmark porous material Basotect G+**

  Figs. 14–17 and Appendix B allow us to compare, in addition to the benchmark (1 × 1) basic MPPA, the performance of the MC-MPPA with the industry standard Basotect G+. As expected, the performance of Basotect G+ improves with increasing depth, but for any particular depth, its absorption coefficient is always significantly less than that of the MC-MPPA.

  Comparing Basotect with the (1 × 1) basic MPPA, it generally performs worse, as the Basotect material does not lend itself to optimisation using the TpIM routine. However, it is most likely that Basotect performs better than many unoptimised examples of the basic (1 × 1) MPPA to be found in the literature. An exception to this observation with the current data is that Basotect is better than the (1 × 1) MPPA for the deepest examples for the larger pore diameter range where the (1 × 1) MPPA underperforms.

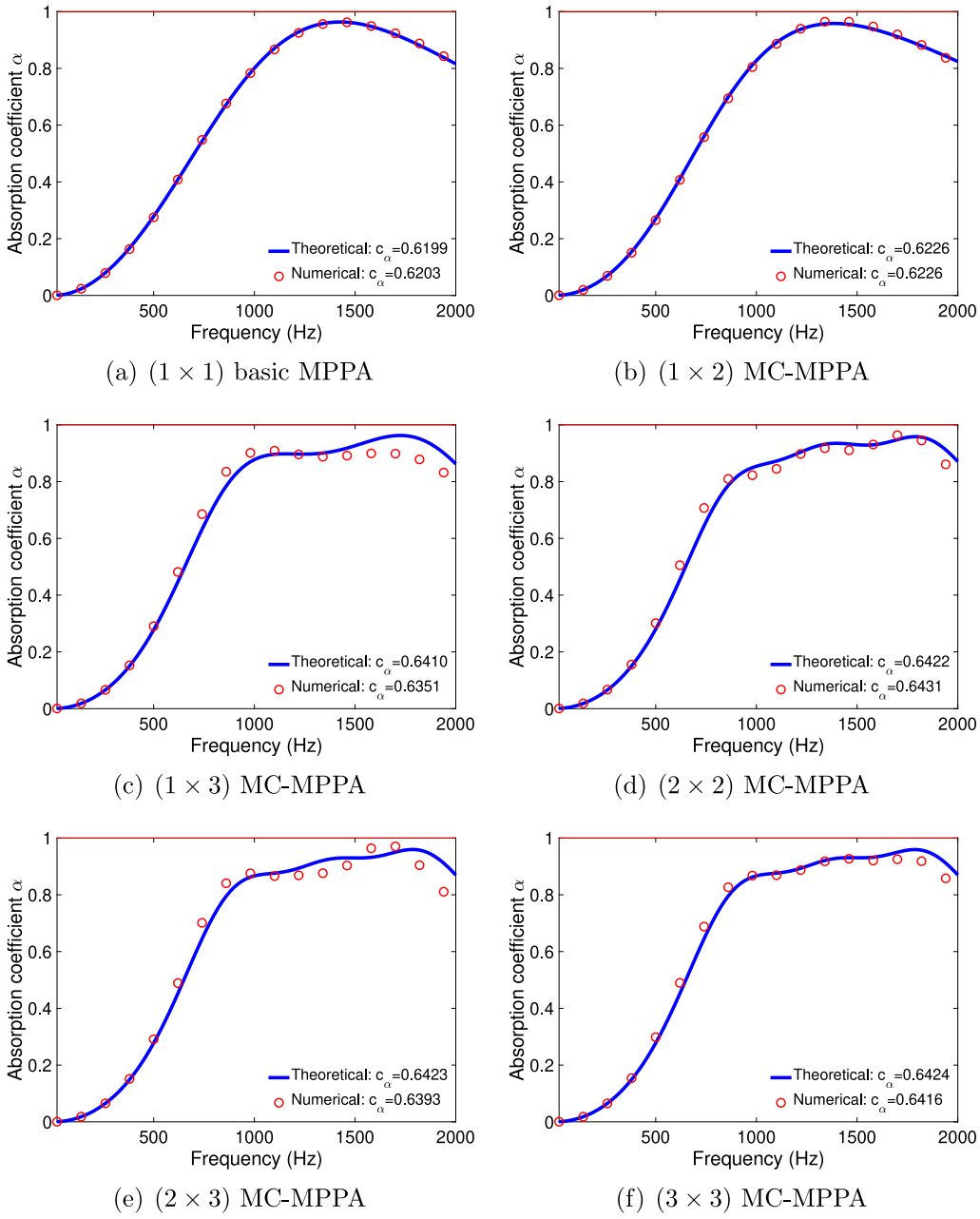

Fig. 18. Analytical (TpIM) and numerical sound absorption coefficients. D = 25 mm.

Again, as the Basotect material does not lend itself to optimisation using the TpIM routine, it cannot be optimised to attenuate tones, and therefore when tones exist at low frequencies, the only approach with Basotect is to dramatically increase its depth. This underscores the significant advantage of the optimised MC-MPPA over basic porous materials. Comparing the results for the (3 × 3) MC-MPPA to Basotect in Fig. 17 is stark.

- **Numerical Validation**

  Referring to Fig. 18, we see a comparison of the numerical results versus the analytical TpIM for the six configurations in Fig. 1 for a white noise case. Overall the agreement is very satisfactory and is sufficiently close to allow us to state, in addition to the comparisons made in Fig. 7, that the TpIM approach is validated for both the optimised conditions and for higher-order chamber configurations. Allowing ourselves to inspect a bit more closely, we see that there is a slight deterioration with increasing frequency in (1 × 3), (2 × 3) and (3 × 3) cases. It is not quite as straightforward to say that the disagreement is a function of the number of chambers as the (3 × 3) case seems to be more accurate than the (1 × 3) case. As the depth of this

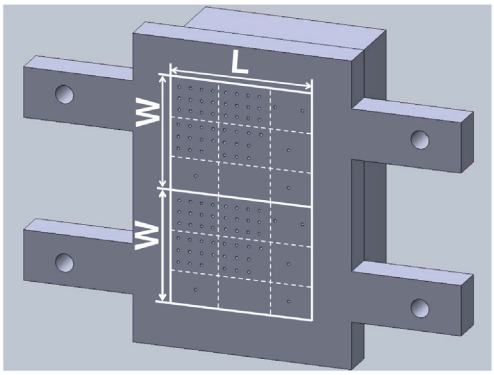

(a) Top view of the MC-MPPA showing the perforations in the MPPt. This is the side exposed to the acoustic plane waves in the impedance tube.

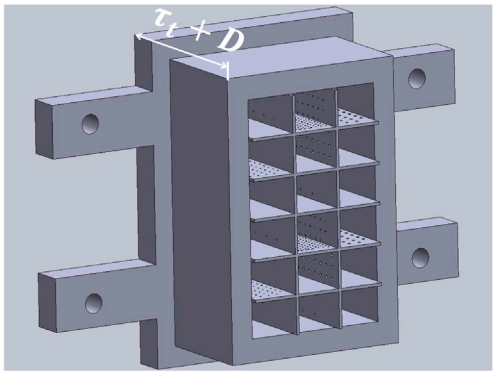

(b) View of the internal perforated panels. Hole number and porosity can vary from panel to panel. A solid backing is attached to this side.

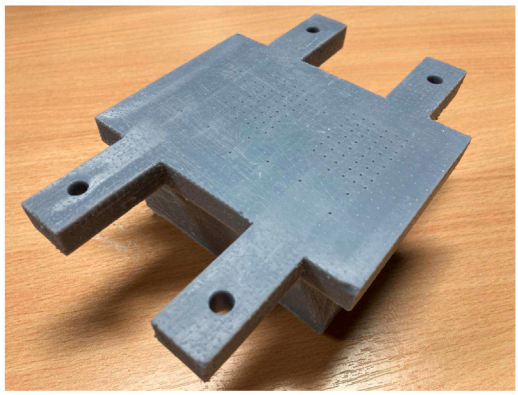

(c) Photograph of MC-MPPA with rig attachment flanges.

Fig. 19. CAD and photo images of test sample 50 MC-MPPA.

test case is only 25 mm, the slight error is very unlikely to be attributable to a violation of the lumped element application but perhaps the porosity of the holes is such that hole-to-hole spacing is not negligible at higher frequencies. Further investigation will be conducted to try and understand the small discrepancy.

- **Experimental Validation**

  Referring to Fig. 23, the absorption curve for the experimental results is nearly identical to those of the numerical results. Comparing these results with the analytical results, there is a slight deviation above 700 Hz, which may be caused by a violation of the lumped element approximation as the air cavity depth is 50 mm in this Test sample 50. However, the close agreement of the experimental results to both the analytical and numerical results demonstrates the viability of the technology. For Test sample 50, the overall sound absorption coefficient c_α in the 200 Hz to 1000 Hz range for the analytical, numerical and experimental analyses, are 0.8071, 0.7843 and 0.7720, respectively. When the frequency is greater than 281 Hz, which is the frequency at which the absorption coefficient increases above 0.5, Test sample 50 performs particularly well (analytical c_α: 0.8692 numerical c_α: 0.8444 and experimental c_α: 0.8225) the response of the MC-MPPA being essentially continuously broadband. The identically-sized Basotech G+'s measured absorption coefficient, on the other hand, is only 0.6177 between 200 Hz and 2000 Hz and 0.6496 between 281 Hz and 2000 Hz.

  Referring to Fig. 24, in the 200 Hz to 2000 Hz frequency range examined for the very thin Test Sample 20, the overall sound absorption coefficient c_α from the analytical, numerical and experimental analyses are 0.6746, 0.6686 and 0.6703, respectively. When the frequency is greater than 660 Hz, Test sample 20 performs particularly well (analytical c_α: 0.8586, numerical c_α: 0.8428 and experimental c_α: 0.8273). On the other hand, for the same thickness of the absorber, Basotech G+'s measured absorption coefficient is only 0.4605 between 200 Hz and 2000 Hz and 0.5470 between 660 Hz and 2000 Hz. In addition, there is a good agreement for this sample between all of the analytical, numerical and experimental results. As the sample is so thin, there appears to be no issue with the lumped element assumption at the higher frequency end.

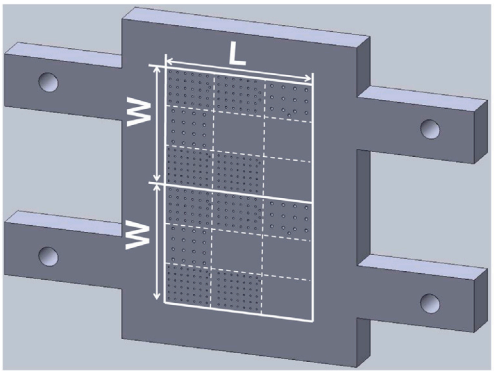

(a) Top view of the MC-MPPA showing the perforations in the MPPt. This is the side exposed to the acoustic plane waves in the impedance tube.

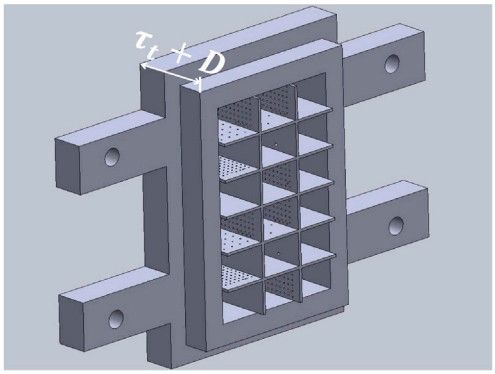

(b) View of the internal perforated panels. Hole number and porosity can vary from panel to panel. A solid backing is attached to this side.

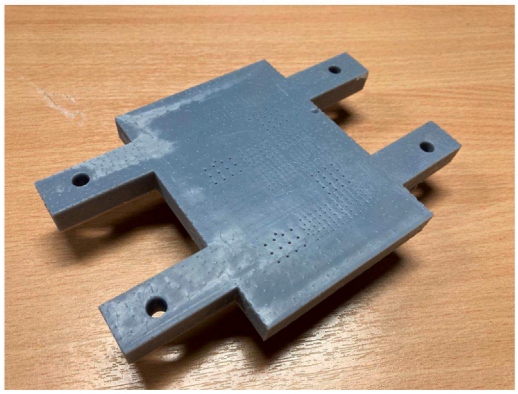

(c) Photograph of MC-MPPA with rig attachment flanges.

Fig. 20. CAD and photo images of test sample 20 MC-MPPA.

- **Comparison of the sound absorption properties of the (3 × 3) MC-MPPA with and without perforated internal panels.** An additional set of tests was performed to evaluate the benefit of the perforated internal walls. Figs. 25 and 26 show the results of the comparison for both the white noise and fan noise cases for the (3 × 3) MC-MPPA which has the most internal walls of the configurations examined. An initial observation is that when there are no perforations in the internal panels the results are quite good. This clearly emphasises the fact that the optimised TpIM method is a powerful tool which can be used to maximise the potential of such technologies. When internal panel perforations are included in the model and optimisation routine, Fig. 25 shows that these perforations serve to broaden the response when white noise is the source. In addition, when tonal noise is the source, the perforations allow additional peaks to be attenuated.

8. Conclusions

1. **The TpIM approach allows MPPA absorbers to be modelled analytically and optimised**
   In this work, an alternative to the equivalent circuit model method based on electro-acoustic analogies is presented. This alternative, based on graph theory, is called the Two-Point Impedance Method and has been transferred from the electronics domain to the acoustics domain in this work and applied to the MPPA technology. This improved method allows single (1 × 1) MPPAs, or a group of six (1 × 1) MPPAs (which is the case of the (3 × 3) MC-MPPA without internal perforations, to be optimised, resulting in a broader band response than is typically found in the literature. In addition, MC-MPPAs have been studied analytically. The development of the TpIM approach facilitates the examination of single chamber MPPAs tessellated alongside one another and separated by perforated walls in two dimensions, which is unmanageable using the ECM method, and allows for an optimisation of the system parameters, such as hole diameter and porosity, to be performed.

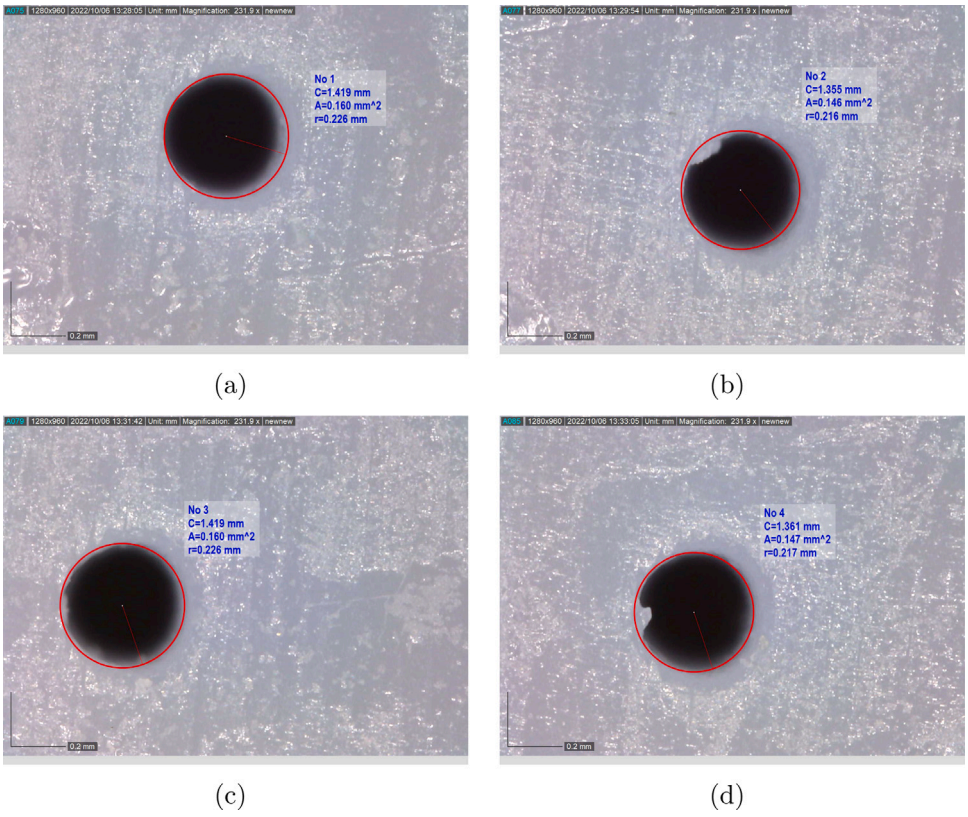

Fig. 21. Microscope images of four randomly chosen 0.5 mm-diameter 3D-printed holes from test samples, where r represents the radius of the hole, A represents the area of the hole, and C represents the perimeter of the hole.

The TpIM has been successfully validated against the ECM method, numerical results and results to be found in the literature for (1 × 2) and (1 × 3) chambers and also against numerical results for (1 × 1), (1 × 2), (1 × 3), (2 × 2), (2 × 3) and (3 × 3) MC-MPPAs. The TpIM has also been successfully validated against experimental data for the (3 × 3) MC-MPPA with white noise source.

2. **In addition to white noise, tonal noise can be attenuated with the MC-MPPA**
   In this paper, the capacity of the TpIM to be applied to target noise sources containing multiple tones, which is an important scientific challenge, has also been successfully demonstrated. By increasing the number of chambers, the MC-MPPA is increasingly able to attenuate additional tones, with, for the Case 4 example given in this paper, the majority of fan noise being attenuated by the (3 × 3) MC-MPPA for air cavity depths greater than 20 mm.
   In addition to the benefit arising from an increase in chambers allowing multiple tones to be more efficiently suppressed, increasing the number of chambers improves absorption in general, with the value of the overall absorption coefficient, c_α, being better than the (1 × 1) MPPA for almost all of the configurations examined with the greatest improvement being 0.91 (3 × 3) versus 0.67 (1 × 1) for an overall thickness of 42 mm for Case 4.
3. **Pore diameter can have an effect on the sound absorption performance of an MPPA for different target sources and different numbers of cavities.**
   The literature reports pore diameters to a micron level numerically, whereas there are still challenges to manufacturing such small sizes practically. As a result of this, this research examines two principal pore size ranges: [0.05–0.3] mm and [0.3 - 1] mm. In general, for a white noise source, a decrease in the pore size results in an increase in the absorption coefficient and a broadening of the frequency range for the basic (1 × 1) MPPA, which is in agreement with Maa [1]. For the MC-MPPA, an increase in pore diameter allows slightly lower frequencies to be attenuated and results in perturbations in the response. When the noise source is tonal, there is no change in the response of the (1 × 1) MPPA, demonstrating that it is unable to target tones. For the MC-MPPAs, an increase in pore diameter benefits the attenuation of tones. The interesting conclusion from this study is that, for the MC-MPPA with both white noise and tonal noise sources, there is no need to manufacture micron-level holes, as it appears that the perforated internal panels and the optimisation are sufficient to maximise performance.
4. **Perforated internal panels allow tones to be absorbed and increase frequency bandwidth response.**
   The MC-MPPA is capable of attenuating specific acoustic tones whereas the (1 × 1) MPPA is not. In addition, for tessellated MPPAs, perforated panels are more capable of attenuating tones than solid internal panels and they increase absorption bandwidth. This offers new approaches for the attenuation of industrial fan noise, domestic appliances and aeroengines [50].

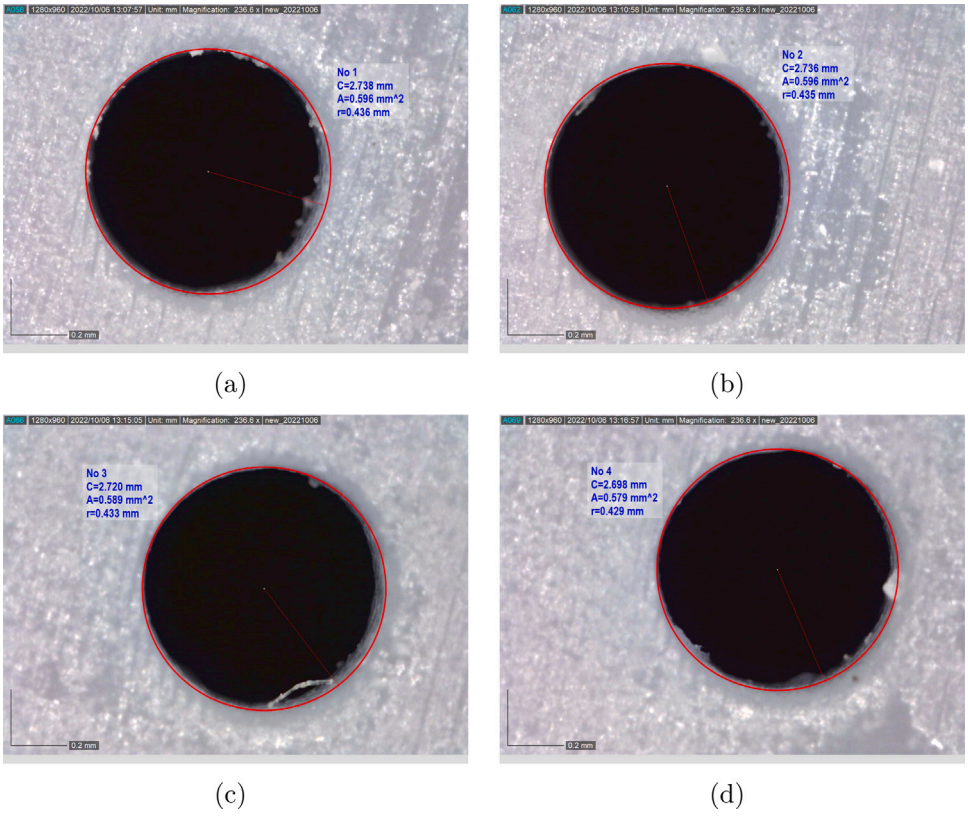

Fig. 22. Microscope images of four randomly chosen 0.9 mm-diameter 3D-printed holes from test samples, where r represents the radius of the hole, A represents the area of the hole, and C represents the perimeter of the hole.

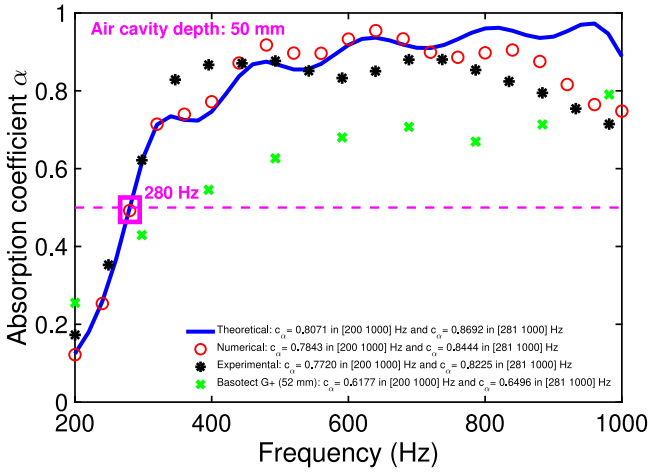

Fig. 23. Test sample 50's analytical (TpIM), numerical and experimental sound absorption coefficients. D = 50 mm. Target spectrum: white noise; Perforation porosity range: [0-5] %; frequency range: [200 1000] Hz. Basotect G+ result shown for comparison.

5. **The MC-MPPA can provide broadband, low-frequency (below 1000 Hz), broadband noise attenuation**
   Effective low-frequency, broadband noise absorption is an intractable challenge. The optimised (3 × 3) MC-MPPA, for an air cavity depth of as little as 50 mm, achieves an absorption coefficient of 0.77 between 200 Hz and 1000 Hz, or 0.83 between 281 Hz and 1000 Hz. This result has been achieved experimentally.

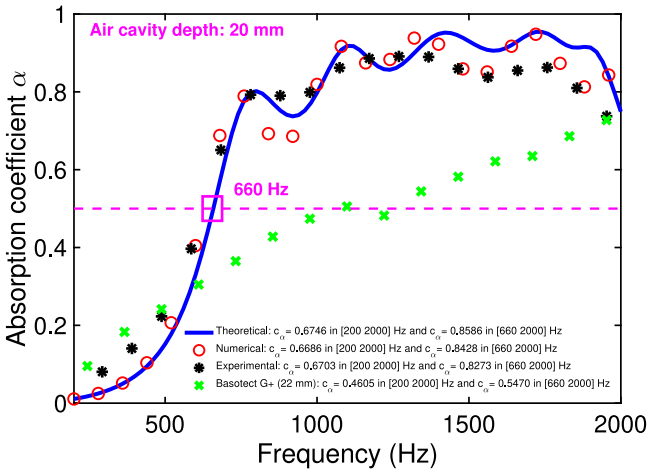

Fig. 24. Test sample 20's analytical (TpIM), numerical and experimental sound absorption coefficients. D = 20 mm. Target spectrum: white noise; Perforation porosity range: [0-5] %; frequency range: [200 2000] Hz. Basotect G+ result shown for comparison.

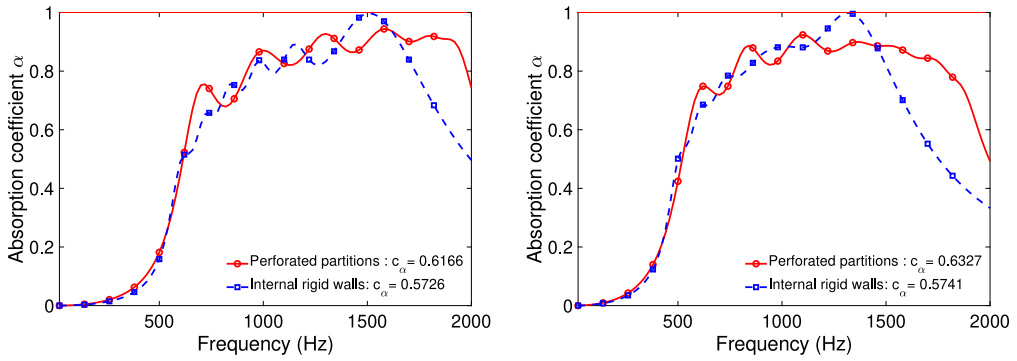

(a) air cavity depth: 20 mm, overall absorber thickness: 22 mm

(b) air cavity depth: 25 mm, overall absorber thickness: 27 mm

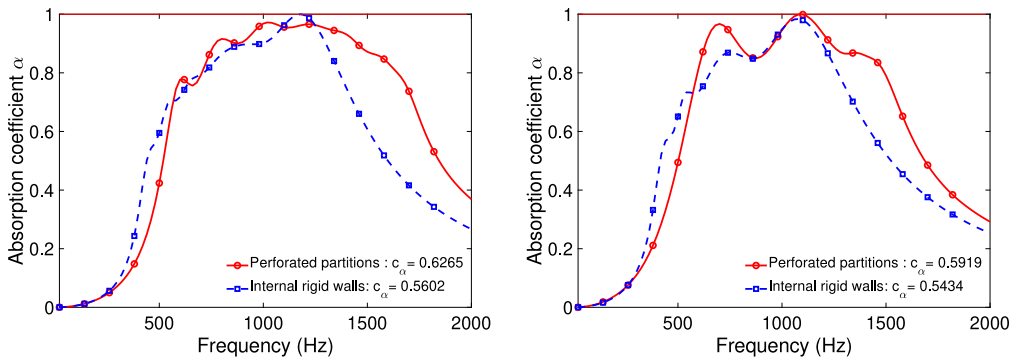

(c) air cavity depth: 30 mm, overall absorber thickness: 32 mm

(d) air cavity depth: 35 mm, overall absorber thickness: 37 mm

Fig. 25. Sound absorption coefficients of optimised (3 × 3) MC-MPPA with and without perforated internal panels, frequency range: [20 2000] Hz, target spectrum: white noise, perforations diameter range: [0.5 1.0] mm and perforations porosity range: [0 5]%, L = 50 mm, W = 40 mm..

6. **The MC-MPPA performs significantly better than benchmark alternatives.**
   The MC-MPPA significantly outperforms both the basic (1 × 1) MPPA and Basotect G+, which is an industry-standard melamine resin foam. The MC-MPPA also performs better than a 2DOF MPPA (MPP1+air layer 1+MPP2+air layer 2) which can be found in the Supplementary Materials.

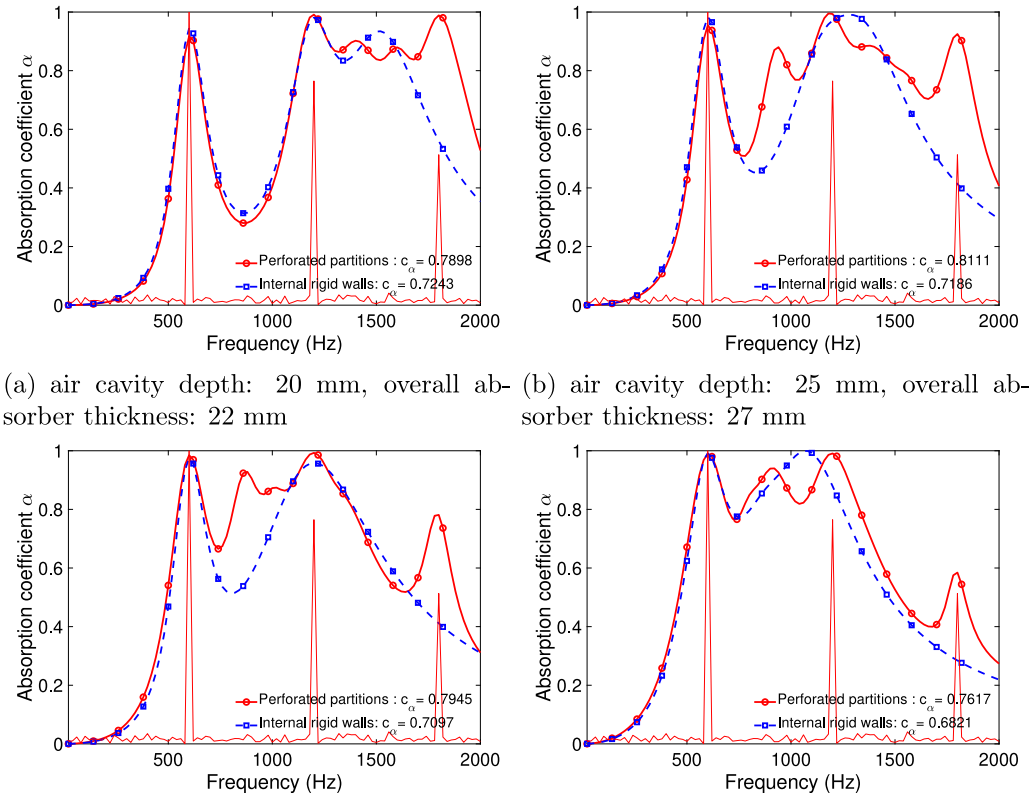

(a) air cavity depth: 20 mm, overall absorber thickness: 22 mm

(b) air cavity depth: 25 mm, overall absorber thickness: 27 mm

(c) air cavity depth: 30 mm, overall absorber thickness: 32 mm

(d) air cavity depth: 35 mm, overall absorber thickness: 37 mm

Fig. 26. Sound absorption coefficients of optimised (3 × 3) MC-MPPA with and without perforated internal panels, frequency range: [20 2000] Hz, target spectrum: fan noise, perforations diameter range: [0.5 1.0] mm and perforations porosity range: [0 5]%, L = 50 mm, W = 40 mm.

7. **The MC-MPPA is a deeply sub-wavelength broadband noise sound absorber.**
   Analytically, perfect attenuation at 600 Hz is achieved at a depth of 42 mm, which is a depth-to-wavelength ratio of 14. Experimentally, an absorption coefficient of approximately 0.82 is achieved at 340 Hz at a depth of 52 mm, which is a depth-to-wavelength ratio of 20.

CRediT authorship contribution statement

Jiayu Wang: Investigation, Conceptualization, Methodology, Software, Data curation, Visualization, Writing – original draft, Writing – review & editing. **Gareth J. Bennett:** Methodology, Software, Conceptualization, Writing – final draft, Writing – review & editing, Resources, Supervision.

Declaration of competing interest

The authors declare that they have no known competing financial interests or personal relationships that could have appeared to influence the work reported in this paper.

Data availability

Data will be made available on request.

Acknowledgements

This project has received funding from the European Union's Horizon 2020 research and innovation programme under grant agreement No 860538. Jiayu Wang is supported by the China Scholarship Council (CSC) – Trinity College Dublin Joint Scholarship Programme. The authors would also like to thank Eoghan Ross (Fluids Lab, Trinity College Dublin) for his support with the 3D printing and experiments and Jack Killeen (Intel Corporation) for his help in drawing Fig. 5(a).

Table B.5
Overall sound absorption coefficient c_α for Case 1, absorber thickness: [12 42] mm, air-back cavity depth: [10 40] mm, frequency range: [200 2000] Hz (For the reader's comparison, the maximum overall absorption coefficient is bolded for each air back cavity depth).

Absorber thickness (mm)	(1 × 1)	(1 × 2)	(1 × 3)	(2 × 2)	(2 × 3)	(3 × 3)	Basotect G+
12	0.4782	**0.4862**	0.4856	0.4850	0.4786	0.4787	0.2992
17	0.5675	0.5846	0.5845	**0.5847**	0.5845	0.5845	0.4003
22	0.6313	0.6523	0.6526	0.6531	**0.6533**	**0.6533**	0.4605
27	0.6797	0.6829	0.7032	0.7046	0.7047	**0.7048**	0.5371
32	0.7178	0.7212	0.7441	0.7420	0.7443	**0.7448**	0.6023
37	0.7485	0.7664	0.7760	0.7751	0.7768	**0.7770**	0.6515
42	0.7736	0.7858	0.7890	0.7904	**0.7936**	**0.7936**	0.6869

Table B.6
Overall sound absorption coefficient c_α in Case 2, absorber thickness: [12 42] mm, air-back cavity depth: [10 40] mm, frequency range: [200 2000] Hz (For the reader's comparison, the maximum overall absorption coefficient is bolded for each air back cavity depth).

Absorber thickness (mm)	(1 × 1)	(1 × 2)	(1 × 3)	(2 × 2)	(2 × 3)	(3 × 3)	Basotect G+
12	0.4778	0.4778	0.4778	**0.5242**	0.4781	0.4778	0.2992
17	0.5558	0.5558	0.5558	0.5995	**0.6168**	0.6142	0.4003
22	0.6000	0.6000	0.6610	0.6590	0.6770	**0.6772**	0.4605
27	0.6254	0.7008	0.7004	0.7036	0.7291	**0.7311**	0.5371
32	0.6395	0.7340	0.7538	0.7555	0.7648	**0.7690**	0.6023
37	0.6462	0.7539	0.7787	0.7916	0.7929	**0.7957**	0.6515
42	0.6476	0.7555	0.7896	0.7628	0.8014	**0.8022**	0.6869

Appendix A. Equivalent circuits simplification of 1 × 3 chambers MPPA

Fig. 2(b) shows equivalent circuit models 1 × 3 chambers MPPA. The following is its simplified process.

$$
\begin{aligned}
Z_A &= \frac{Z_{12}Z_{13}}{Z_{12}+Z_{13}+Z_{23}} \\
Z_B &= \frac{Z_{12}Z_{23}}{Z_{12}+Z_{13}+Z_{23}} \\
Z_C &= \frac{Z_{13}Z_{23}}{Z_{12}+Z_{13}+Z_{23}}
\end{aligned}
\tag{A.1}
$$

$$
\begin{aligned}
Z_{A1} &= \frac{(Z_B+Z_{26})Z_C}{(Z_B+Z_{26})+Z_C+Z_{36}} \\
Z_{B1} &= \frac{Z_C Z_{36}}{(Z_B+Z_{26})+Z_C+Z_{36}} \\
Z_{C1} &= \frac{(Z_B+Z_{26})Z_{36}}{(Z_B+Z_{26})+Z_C+Z_{36}}
\end{aligned}
\tag{A.2}
$$

$$
\begin{aligned}
Z_{A2} &= \frac{Z_{C1}Z_{46}}{(Z_{B1}+Z_{34})+Z_{C1}+Z_{46}} \\
Z_{B2} &= \frac{Z_{C1}(Z_{B1}+Z_{34})}{(Z_B+Z_{26})+Z_C+Z_{36}} \\
Z_{C2} &= \frac{(Z_{B1}+Z_{34})Z_{46}}{(Z_B+Z_{26})+Z_C+Z_{36}}
\end{aligned}
\tag{A.3}
$$

In Fig. 2(b), the acoustic impedance between nodes 1 and 5 is given by

$$
Z_{15} = \left(\frac{\left(Z_{14}+Z_{C2}\right)\left(Z_A+Z_{A1}+Z_{B2}\right)}{Z_{14}+Z_{C2}+Z_A+Z_{A1}+Z_{B2}} + Z_{A2} \right) \tag{A.4}
$$

and the specific impedance z_{15} is given by Eq. (7). Then normal incidence sound absorption coefficient α is given by Eqs. (8) and (9).

Appendix B. Overall sound absorption coefficient c_α between 200 Hz to 2 kHz in the four cases in Section 6

See Tables B.5–B.8.

Table B.7
Overall sound absorption coefficient c_α in Case 3, absorber thickness: [12 42] mm, air-back cavity depth: [10 40] mm, frequency range: [200 2000] Hz (For the reader's comparison, the maximum overall absorption coefficient is bolded for each air back cavity depth).

Absorber thickness (mm)	(1 × 1)	(1 × 2)	(1 × 3)	(2 × 2)	(2 × 3)	(3 × 3)	Basotect G+
12	0.4646	0.4750	**0.4788**	**0.4788**	0.4787	**0.4788**	0.2857
17	0.5591	0.5611	**0.5786**	0.5771	0.5785	**0.5786**	0.3893
22	0.6277	0.6301	0.6464	**0.6551**	0.6463	0.6464	0.4431
27	0.6812	0.7016	0.7000	**0.7182**	0.7032	**0.7182**	0.5335
32	0.7242	0.7448	0.7687	0.7688	**0.7694**	0.7669	0.5898
37	0.7592	0.7806	0.7862	0.8106	0.8095	**0.8110**	0.6365
42	0.7878	0.8045	0.8338	0.8374	0.8280	**0.8401**	0.6942

Table B.8
Overall sound absorption coefficient c_α in Case 4, absorber thickness: [12 42] mm, air-back cavity depth: [10 40] mm, frequency range: [200 2000] Hz (For the reader's comparison, the maximum overall absorption coefficient is bolded for each air back cavity depth).

Absorber thickness (mm)	(1 × 1)	(1 × 2)	(1 × 3)	(2 × 2)	(2 × 3)	(3 × 3)	Basotect G +
12	0.4646	0.4646	0.4646	0.5374	0.4660	**0.6510**	0.2857
17	0.5511	0.5511	0.5511	0.6054	**0.7561**	0.6055	0.3893
22	0.6008	0.6008	0.6008	0.6517	0.8169	**0.8192**	0.4431
27	0.6307	0.6307	0.6966	0.8405	0.8530	**0.8538**	0.5335
32	0.6501	0.7374	0.8708	0.8766	0.8778	**0.8793**	0.5898
37	0.6640	0.7643	0.8900	0.8807	**0.9020**	0.8991	0.6365
42	0.6741	0.8199	0.8930	0.8907	0.8986	**0.9056**	0.6942

Table C.9
Geometric parameters of the (3 × 3) MC-MPPA of test sample 50.

Perforation diameter (mm)								
$d_{t(1,1)}$	1.00	$d_{t(1,2)}$	1.00	$d_{t(1,3)}$	1.00	$d_{t(2,1)}$	1.00	$d_{t(2,2)}$	1.00
$d_{t(2,3)}$	1.00	$d_{t(3,1)}$	1.00	$d_{t(3,2)}$	0	$d_{t(3,3)}$	1.00		
$d_{i(1)}$	0.50	$d_{i(2)}$	0.50	$d_{i(3)}$	1.00	$d_{i(4)}$	0.50	$d_{i(5)}$	0
$d_{i(6)}$	0	$d_{i(7)}$	1.00	$d_{i(8)}$	0	$d_{i(9)}$	1.00	$d_{i(10)}$	0.50
$d_{i(11)}$	0.50	$d_{i(12)}$	0.50						
Perforation porosity (%)								
$\varphi_{t(1,1)}$	0.75	$\varphi_{t(1,2)}$	4.54	$\varphi_{t(1,3)}$	4.56	$\varphi_{t(2,1)}$	4.13	$\varphi_{t(2,2)}$	3.97
$\varphi_{t(2,3)}$	0.45	$\varphi_{t(3,1)}$	0.46	$\varphi_{t(3,2)}$	0	$\varphi_{t(3,3)}$	0.43		
$\varphi_{i(1)}$	0.37	$\varphi_{i(2)}$	1.56	$\varphi_{i(3)}$	5.00	$\varphi_{i(4)}$	5.00	$\varphi_{i(5)}$	0
$\varphi_{i(6)}$	0	$\varphi_{i(7)}$	5.00	$\varphi_{i(8)}$	0	$\varphi_{i(9)}$	0.55	$\varphi_{i(10)}$	1.93
$\varphi_{i(11)}$	0.07	$\varphi_{i(12)}$	0.28						

(*continued on next page*)

Table C.9 (*continued*).

Perforation number								
$n_{t(1,1)}$	2	$n_{t(1,2)}$	12	$n_{t(1,3)}$	12	$n_{t(2,1)}$	11	$n_{t(2,2)}$	10
$n_{t(2,3)}$	1	$n_{t(3,1)}$	1	$n_{t(3,2)}$	0	$n_{t(3,3)}$	1		
$n_{i(1)}$	12	$n_{i(2)}$	50	$n_{i(3)}$	51	$n_{i(4)}$	204	$n_{i(5)}$	0
$n_{i(6)}$	0	$n_{i(7)}$	40	$n_{i(8)}$	0	$n_{i(9)}$	6	$n_{i(10)}$	79
$n_{i(11)}$	2	$n_{i(12)}$	9						
Other geometric parameters									
L	50 mm	W	40 mm	D	50 mm	τ_i	1 mm	τ_t	2 mm

Appendix C. Geometric parameters of test samples in the experimental validation

See Tables C.9 and C.10.

Table C.10
Geometric parameters of the (3 × 3) MC-MPPA of test sample 20.

Perforation diameter (mm)									
$d_{t(1,1)}$	0.98	$d_{t(1,2)}$	0.63	$d_{t(1,3)}$	0.64	$d_{t(2,1)}$	0.90	$d_{t(2,2)}$	0
$d_{t(2,3)}$	0	$d_{t(3,1)}$	0	$d_{t(3,2)}$	0.50	$d_{t(3,3)}$	0.50		
$d_{i(1)}$	0.50	$d_{i(2)}$	0.50	$d_{i(3)}$	0	$d_{i(4)}$	0.50	$d_{i(5)}$	0.50
$d_{i(6)}$	0	$d_{i(7)}$	1.00	$d_{i(8)}$	0	$d_{i(9)}$	0	$d_{i(10)}$	0.50
$d_{i(11)}$	0	$d_{i(12)}$	0.51						
Perforation porosity (%)									
$\varphi_{t(1,1)}$	5.00	$\varphi_{t(1,2)}$	5.00	$\varphi_{t(1,3)}$	5.00	$\varphi_{t(2,1)}$	5.00	$\varphi_{t(2,2)}$	0
$\varphi_{t(2,3)}$	0	$\varphi_{t(3,1)}$	0	$\varphi_{t(3,2)}$	4.22	$\varphi_{t(3,3)}$	4.22		
$\varphi_{i(1)}$	5.00	$\varphi_{i(2)}$	5.00	$\varphi_{i(3)}$	0	$\varphi_{i(4)}$	0.58	$\varphi_{i(5)}$	1.47
$\varphi_{i(6)}$	0	$\varphi_{i(7)}$	1.28	$\varphi_{i(8)}$	0	$\varphi_{i(9)}$	0	$\varphi_{i(10)}$	5.00
$\varphi_{i(11)}$	0	$\varphi_{i(12)}$	5.00						
Perforation number									
$n_{t(1,1)}$	13	$n_{t(1,2)}$	32	$n_{t(1,3)}$	31	$n_{t(2,1)}$	16	$\varphi_{t(2,2)}$	0
$n_{t(2,3)}$	0	$n_{t(3,1)}$	0	$n_{t(3,2)}$	43	$n_{t(3,3)}$	43		
$n_{i(1)}$	64	$n_{i(2)}$	64	$n_{i(3)}$	0	$n_{i(4)}$	10	$n_{i(5)}$	24
$n_{i(6)}$	0	$n_{i(7)}$	4	$n_{i(8)}$	0	$n_{i(9)}$	0	$n_{i(10)}$	81
$n_{i(11)}$	0	$n_{i(12)}$	61						
Other geometric parameters									
L	50 mm	W	40 mm	D	20 mm	τ_i	1 mm	τ_t	2 mm

Appendix D. Supplementary data

Supplementary material related to this article can be found online at https://doi.org/10.1016/j.jsv.2022.117527.

References

[1] D.-Y. Maa, Theory and design of microperforated panel sound-absorbing constructions, Sci. Sin. 18 (1975) 55–71, http://dx.doi.org/10.1360/ya1975-18-1-55.
[2] D.-Y. Maa, Microperforated-panel wideband absorbers, Noise Control Eng. J. 29 (1987) 77–84, http://dx.doi.org/10.3397/1.2827694.
[3] D.-Y. Maa, Potential of microperforated panel absorber, J. Acoust. Soc. Am. 104 (5) (1998) 2861–2866, http://dx.doi.org/10.1121/1.423870.
[4] C. Wang, L. Huang, On the acoustic properties of parallel arrangement of multiple micro-perforated panel absorbers with different cavity depths, J. Acoust. Soc. Am. 130 (1) (2011) 208–218, http://dx.doi.org/10.1121/1.3596459.
[5] X. Liu, C. Wang, Y. Zhang, L. Huang, Investigation of broadband sound absorption of smart micro-perforated panel (MPP) absorber, Int. J. Mech. Sci. 199 (2021) 106426, http://dx.doi.org/10.1016/j.ijmecsci.2021.106426.
[6] C. Wang, L. Cheng, J. Pan, G. Yu, Sound absorption of a micro-perforated panel backed by an irregular-shaped cavity, J. Acoust. Soc. Am. 127 (1) (2010) 238–246, http://dx.doi.org/10.1121/1.3257590.
[7] B. Dong, D. Xie, F. He, L. Huang, Noise attenuation and performance study of a small-sized contra-rotating fan with microperforated casing treatments, Mech. Syst. Signal Process. 147 (2021) 107086, http://dx.doi.org/10.1016/j.ymssp.2020.107086.
[8] Y. Zhang, Y.-J. Chan, L. Huang, Thin broadband noise absorption through acoustic reactance control by electro-mechanical coupling without sensor, J. Acoust. Soc. Am. 135 (5) (2014) 2738–2745, http://dx.doi.org/10.1121/1.4871189.
[9] C. Yang, L. Cheng, J. Pan, Absorption of oblique incidence sound by a finite micro-perforated panel absorber, J. Acoust. Soc. Am. 133 (1) (2013) 201–209, http://dx.doi.org/10.1121/1.4768869.
[10] C. Yang, L. Cheng, Sound absorption of microperforated panels inside compact acoustic enclosures, J. Sound Vib. 360 (2016) 140–155, http://dx.doi.org/10.1016/j.jsv.2015.09.024.
[11] X. Li, X. Yu, W. Zhai, Additively manufactured deformation-recoverable and broadband sound-absorbing microlattice inspired by the concept of traditional perforated panels, Adv. Mater. 33 (44) (2021) 2104552, http://dx.doi.org/10.1002/adma.202104552.
[12] T. Bravo, C. Maury, Causally-guided acoustic optimization of single-layer rigidly-backed micro-perforated partitions: theory, J. Sound Vib. 520 (2022) 116634, http://dx.doi.org/10.1016/j.jsv.2021.116634.
[13] T. Bravo, C. Maury, Causally-guided acoustic optimization of rigidly-backed micro-perforated partitions: case studies and experiments, J. Sound Vib. 523 (2022) 116735, http://dx.doi.org/10.1016/j.jsv.2021.116735.
[14] J. Rayleigh, R. Lindsay, The Theory of Sound, second ed., Dover, New York, 1945.
[15] I.B. Crandall, Theory of Vibrating Systems and Sound, Macmillan, London, 1926, p. 272.
[16] H. Ruiz, P. Cobo, F. Jacobsen, Optimization of multiple-layer microperforated panels by simulated annealing, Appl. Acoust. 72 (10) (2011) 772–776, http://dx.doi.org/10.1016/j.apacoust.2011.04.010.
[17] X. Tang, X. Yan, Acoustic energy absorption properties of fibrous materials: A review, Composites A 101 (2017) 360–380, http://dx.doi.org/10.1016/j.compositesa.2017.07.002.
[18] X.-F. Zhu, S.-K. Lau, Z. Lu, W. Jeon, Broadband low-frequency sound absorption by periodic metamaterial resonators embedded in a porous layer, J. Sound Vib. 461 (2019) 114922, http://dx.doi.org/10.1016/j.jsv.2019.114922.
[19] A. McKay, I. Davis, J. Killeen, G.J. Bennett, SeMSA: a compact super absorber optimised for broadband, low-frequency noise attenuation, Sci. Rep. 10 (1) (2020) 17967, http://dx.doi.org/10.1038/s41598-020-73933-0.
[20] Z. Yang, J. Mei, M. Yang, N.H. Chan, P. Sheng, Membrane-type acoustic metamaterial with negative dynamic mass, Phys. Rev. Lett. 101 (2008) 204301, http://dx.doi.org/10.1103/PhysRevLett.101.204301.
[21] G. Ma, M. Yang, S. Xiao, Z. Yang, P. Sheng, Acoustic metasurface with hybrid resonances, Nature Mater. 13 (9) (2014) 873–878, http://dx.doi.org/10.1038/nmat3994.

[22] J. Mei, G. Ma, M. Yang, Z. Yang, W. Wen, P. Sheng, Dark acoustic metamaterials as super absorbers for low-frequency sound, Nature Commun. 3 (1) (2012) 756, http://dx.doi.org/10.1038/ncomms1758.
[23] M.R. Khosravani, T. Reinicke, Experimental characterization of 3D-printed sound absorber, J. Mech. 89 (2021) 104304, http://dx.doi.org/10.1016/j.euromechsol.2021.104304.
[24] H. Min, W. Guo, Sound absorbers with a micro-perforated panel backed by an array of parallel-arranged sub-cavities at different depths, Appl. Acoust. 149 (2019) 123–128, http://dx.doi.org/10.1016/j.apacoust.2019.01.013.
[25] F. Bucciarelli, G.P. Malfense Fierro, M. Meo, A multilayer microperforated panel prototype for broadband sound absorption at low frequencies, Appl. Acoust. 146 (2019) 134–144, http://dx.doi.org/10.1016/j.apacoust.2018.11.014.
[26] S. Wang, F. Li, A broadband sound absorber of hybrid-arranged perforated panels with perforated partitions, Appl. Acoust. 188 (2022) 108547, http://dx.doi.org/10.1016/j.apacoust.2021.108547.
[27] K.H. Kim, G.H. Yoon, Absorption performance optimization of perforated plate using multiple-sized holes and a porous separating partition, Appl. Acoust. 120 (2017) 21–33, http://dx.doi.org/10.1016/j.apacoust.2017.01.004.
[28] J. Carbajo, J. Ramis, L. Godinho, P. Amado-Mendes, Perforated panel absorbers with micro-perforated partitions, Appl. Acoust. 149 (2019) 108–113, http://dx.doi.org/10.1016/j.apacoust.2019.01.023.
[29] C. Wang, X. Liu, Investigation of the acoustic properties of corrugated micro-perforated panel backed by a rigid wall, Mech. Syst. Signal Process. 140 (2020) 106699, http://dx.doi.org/10.1016/j.ymssp.2020.106699.
[30] D.Y. Kong, D.Y. Xie, X.N. Tang, M. Hu, H. Xu, Y.J. Qian, Experimental study of a compact piezoelectric micro-perforated panel absorber with adjustable acoustic property, J. Acoust. Soc. Am. 147 (3) (2020) EL283–EL288, http://dx.doi.org/10.1121/10.0000950.
[31] S. Ren, L. Van Belle, C. Claeys, F. Xin, T. Lu, E. Deckers, W. Desmet, Improvement of the sound absorption of flexible micro-perforated panels by local resonances, Mech. Syst. Signal Process. 117 (2019) 138–156, http://dx.doi.org/10.1016/j.ymssp.2018.07.046.
[32] Y. Qian, D. Kong, S. Liu, S. Sun, Z. Zhao, Investigation on micro-perforated panel absorber with ultra-micro perforations, Appl. Acoust. 74 (7) (2013) 931–935, http://dx.doi.org/10.1016/j.apacoust.2013.01.009.
[33] J. Carbajo, J. Ramis, L. Godinho, P. Amado-Mendes, Assessment of methods to study the acoustic properties of heterogeneous perforated panel absorbers, Appl. Acoust. 133 (2018) 1–7, http://dx.doi.org/10.1016/j.apacoust.2017.12.001.
[34] I. Davis, A. McKay, G.J. Bennett, A graph-theory approach to optimisation of an acoustic absorber targeting a specific noise spectrum that approaches the causal optimum minimum depth, J. Sound Vib. 505 (2021) 116135, http://dx.doi.org/10.1016/j.jsv.2021.116135.
[35] W.J. Tzeng, F.Y. Wu, Theory of impedance networks: the two-point impedance and LC resonances, J. Phys. A: Math. Gen. 39 (27) (2006) 8579–8591, http://dx.doi.org/10.1088/0305-4470/39/27/002.
[36] B. Pardowitz, U. Tapken, K. Knobloch, F. Bake, E. Bouty, I. Davis, G.J. Bennett, Core noise - Identification of broadband noise sources of a turbo-shaft engine, in: 20th AIAA/CEAS Aeroacoustics Conference, American Institute of Aeronautics and Astronautics, Atlanta, GA, USA, 2014, http://dx.doi.org/10.2514/6.2014-3321.
[37] K. Zhao, P. Okolo, E. Neri, P. Chen, J. Kennedy, G.J. Bennett, Noise reduction technologies for aircraft landing gear - A bibliographic review, Prog. Aerosp. Sci. 112 (2019) 100589, http://dx.doi.org/10.1016/j.paerosci.2019.100589.
[38] Y. Wang, K. Zhao, X.-Y. Lu, Y.-B. Song, G.J. Bennett, Bio-inspired aerodynamic noise control: a bibliographic review, Appl. Sci. 9 (11) (2019) 2224, http://dx.doi.org/10.3390/app9112224.
[39] F.Y. Wu, Theory of resistor networks: the two-point resistance, J. Phys. A: Math. Gen. 37 (26) (2004) 6653–6673, http://dx.doi.org/10.1088/0305-4470/37/26/004.
[40] ISO 10534-2:1998 Acoustics — Determination of Sound Absorption Coefficient and Impedance in Impedance Tubes — Part 2: Transfer-Function Method, Technical Report, 1998.
[41] A.T. Chambers, J.M. Manimala, M.G. Jones, Design and optimization of 3D folded-core acoustic liners for enhanced low-frequency performance, AIAA J. 58 (1) (2020) 206–218, http://dx.doi.org/10.2514/1.J058017.
[42] D.T. Farrell, C. McGinn, G.J. Bennett, Extension twist deformation response of an auxetic cylindrical structure inspired by deformed cell ligaments, Compos. Struct. 238 (2020) 111901, http://dx.doi.org/10.1016/j.compstruct.2020.111901.
[43] G.J. Bennett, R. Hossain, A. McKay, E.P. Ross, Acoustic diode metamaterial for sound absorption, in: 25th AIAA/CEAS Aeroacoustics Conference, American Institute of Aeronautics and Astronautics, Delft, The Netherlands, 2019, https://arc.aiaa.org/doi/10.2514/6.2019-2422.
[44] J. Killeen, I. Davis, J. Wang, G.J. Bennett, Fan-noise reduction of data-center telecommunications' server racks, with an acoustic metamaterial broadband, low frequency sound absorbing liner, Appl. Acoust. (2022) in press.
[45] X. Xiang, X. Wu, X. Li, P. Wu, H. He, Q. Mu, S. Wang, Y. Huang, W. Wen, Ultra-open ventilated metamaterial absorbers for sound-silencing applications in environment with free air flows, Extreme Mech. Lett. 39 (2020) 100786, http://dx.doi.org/10.1016/J.EML.2020.100786.
[46] A. Rohatgi, Webplotdigitizer: Version 4.5, 2021, https://automeris.io/WebPlotDigitizer.
[47] P.T. Boggs, J.W. Tolle, Sequential quadratic programming, Acta Numer. 4 (1995) 1–51, http://dx.doi.org/10.1017/S0962492900002518.
[48] P.T. Boggs, J.W. Tolle, Sequential quadratic programming for large-scale nonlinear optimization, J. Comput. Appl. Math. 124 (1) (2000) 123–137, http://dx.doi.org/10.1016/S0377-0427(00)00429-5.
[49] J. Kennedy, L. Flanagan, L. Dowling, G.J. Bennett, H. Rice, D. Trimble, The influence of additive manufacturing processes on the performance of a periodic acoustic metamateria, Int. J. Polym. Sci. 2019 (2019) 1–11, http://dx.doi.org/10.1155/2019/7029143.
[50] G.J. Bennett, J. Fitzpatrick, Noise-source identification for ducted fan systems, AIAA J. 46 (7) (2008) http://arc.aiaa.org/doi/abs/10.2514/1.33522.